

# Star formation, morphologies and clustering of galaxies in a radio galaxy protocluster at $z = 4.1^{1,2}$ .

Roderik A. Overzier<sup>3</sup>, R.J. Bouwens<sup>4</sup>, N.J.G. Cross<sup>5</sup>, B. Venemans<sup>6</sup>, G. K. Miley<sup>3</sup>, A.W. Zirm<sup>7</sup>, N. Benítez<sup>8</sup>, J.P. Blakeslee<sup>7</sup>, D. Coe<sup>8</sup>, R. DeMarco<sup>7</sup>, H. Ford<sup>7</sup>, N. Homeier<sup>7</sup>, G.D. Illingworth<sup>4</sup>, J.D. Kurk<sup>9</sup>, A. Martel<sup>7</sup>, S. Mei<sup>7</sup>, H.J.A. Röttgering<sup>3</sup>, Z. Tsvetanov<sup>7,10</sup>, W. Zheng<sup>7</sup>

## ABSTRACT

We present deep  $g_{475}r_{625}i_{775}z_{850}K_S$  observations towards the radio galaxy TN J1338–1942 at  $z = 4.1$ . The radio galaxy is a  $\sim 6L_{z=4}^*$  galaxy. The data allow us to study in detail 12 spectroscopically confirmed companions previously found through their excess Ly $\alpha$  emission by Venemans et al. (2002). We conclude that the Ly $\alpha$  emitters (LAEs) are young (a few  $\times 10^7$  yr), dust-free galaxies based on small sizes, steep UV slopes ( $\beta \approx -2$ ) and blue UV-optical colors with star formation rates (SFRs) of  $< 14 M_\odot \text{ yr}^{-1}$ . When stacking the  $K_S$ -band fluxes, the LAEs seem to be less massive (masses of a few  $\times 10^8 M_\odot$ ) than UV-selected Lyman break galaxies (LBGs) while having comparable UV SFRs. We estimate the LAE AGN fraction to be minimal.

The field further contains 66  $g_{475}$ -dropouts to  $z_{850} = 27$  ( $5\sigma$ ), 6 of which are in the LAE sample. Their SFRs, sizes, morphological parameters, UV slope-magnitude and ( $i_{775} - K_S$ ) vs.  $K_S$  color-magnitude relations are all similar to those found for LBGs in the ‘field’. We quantify the number density and cosmic variance of  $z \sim 4$   $g_{475}$ -dropouts extracted from a pixel-by-pixel transformation of the  $B_{435}V_{606}i_{775}z_{850}$  GOODS survey to  $g_{475}r_{625}i_{775}z_{850}$ , and show that the field of TN J1338–1942 is richer than the average field at the  $> 5\sigma$  significance. The angular distribution is highly filamentary, with about half of the objects clustered in a 4.4 arcmin $^2$  region that includes the radio galaxy and the brightest LBGs. A second, but much less pronounced concentration of objects is seen around another  $\sim 6L^*$  LBG located within the same field, for which we obtained a spectroscopic redshift of  $z = 3.8$ . The generally fainter LAEs appear to favour regions that are devoid of LBGs, while LBGs detected in the rest-frame optical ( $K_S$ ) tend to lie in the richest region, suggesting a forming age- or mass-density relation. We compare the angular two-point correlation function,  $w(\theta)$ , to the signal measured in similarly sized mock samples with a built-in two-point clustering as measured for field LBGs at  $z \sim 4$ . We find an excess signal ( $2\sigma$ ) at separations of  $\theta < 10''$ , corresponding to the typical halo size of dark matter halos hosting bright LBGs. The large galaxy overdensity, its corresponding mass overdensity and the sub-clustering at the approximate redshift of TN J1338–1942 suggest the assemblage of a  $> 10^{14} M_\odot$  structure, possibly a ‘protocluster’.

*Subject headings:* cosmology: observations – early universe – large-scale structure of universe – galaxies: high-redshift – galaxies: clusters: general – galaxies: starburst – galaxies: individual (TN J1338–1942)

<sup>1</sup>Based on observations made with the NASA/ESA Hubble Space Telescope, which is operated by the Association of Universities for Research in Astronomy, Inc., under NASA contract NAS 5-26555. These observations are associated with program # 9291.

<sup>2</sup>Based on observations carried out at the European

Southern Observatory, Paranal, Chile, programs 071.A-0495(A) and 073.A-0286(A).

<sup>3</sup>Leiden Observatory, Postbus 9513, 2300 RA Leiden, Netherlands

<sup>4</sup>UCO/Lick Observatory, University of California, Santa Cruz, CA 95064

## 1. Introduction

The complexity of the present-day large-scale structure originates from small seed density fluctuations, as evidenced by the discovery of the minute cosmic microwave background (CMB) anisotropies. The power spectra of the CMB and galaxy redshift surveys have given important clues to the cosmic matter budget, the density field at recombination ( $z \approx 1000$ ) and the development of galaxies and galaxy bias. The emerging picture is that of bound objects, forming on increasingly larger spatial scales due to gravitational instabilities of the cold dark matter (CDM) in a flat,  $\Lambda$ -dominated universe. It is currently believed that the universe was (re-)ionized by the first light of stars and/or quasars at  $z \sim 7 - 25$  (Kogut et al. 2003).

Large samples of UV-selected Lyman break galaxies (LBGs; masses of a few  $\times 10^{10} M_\odot$  (Papovich et al. 2001; Barmby et al. 2004)) at  $3 < z < 5$  have been used to determine the cosmic star formation rate density well beyond  $z \sim 2$  (e.g. Madau et al. 1996; Steidel et al. 1996, 1999; Ouchi et al. 2004b). LBGs, as well as the partially overlapping population of Ly $\alpha$  emitters (LAEs), are strongly clustered at  $z = 3 - 5$ , and are highly biased relative to predictions for the dark matter distribution (Giavalisco et al. 1998; Adelberger et al. 1998; Ouchi et al. 2004b; Lee et al. 2005; Kashikawa et al. 2005). The biasing becomes stronger for galaxies with higher rest-frame UV luminosity (Giavalisco & Dickinson 2001). In an all-encompassing census of the clustering properties of LBGs, Ouchi et al. (2004b) found that the bias may also increase with redshift and dust extinction. They suggest that the reddest LBGs could be connected with the similarly strong clustered

sub-mm sources (but see Webb et al. 2003) or the extremely red objects (EROs, Elston et al. 1988; McCarthy et al. 2001; Daddi et al. 2002). By comparing the number densities of LBGs to that of dark halos predicted by Sheth & Tormen (1999), they concluded that  $z = 4$  LBGs are hosted by halos of  $1 \times 10^{11} - 5 \times 10^{12} M_\odot$ , and that the descendants of those halos at  $z = 0$  have masses that are comparable to the masses of groups and clusters. The derived halo occupation numbers of LBGs increase with luminosity from a few tenths to roughly unity, implying that there is only one-to-one correspondence between halos and LBGs at the highest masses. On the other hand, the halo occupation numbers of SCUBA sources and distant red galaxies (Franx et al. 2003) are significantly above unity, implying that for a given massive halo only 10% of the galaxies would be identified as an LBG.

The evolution of the earliest objects into present-day galaxies can currently be probed to  $z \sim 7$ , predominantly using the superb resolution and sensitivity of the *Advanced Camera for Surveys* on the *Hubble Space Telescope* (HST/ACS, Ford et al. 1998). The deepest samples of high redshift galaxies currently available come from the Hubble Deep Field North and South (HDFs), the Great Observatories Origins Deep Fields (GOODS) CDF-S and HDF-N, the Hubble Ultra Deep Field (UDF) and the two UDF-Parallel Fields (UDF-Ps). Highlights from these deep studies include the discovery of a population of relatively unreddened, evolved galaxies (having masses of a few  $\times 10^{11} M_\odot$ ) at  $z \sim 2 - 3$  (Franx et al. 2003; van Dokkum et al. 2003, but see Webb et al. (2005)), and the discovery of significant samples of UV-bright  $i_{775}$ -dropouts – galaxies with red enough  $i_{775} - z_{850}$  to lie at  $z \sim 6$  (Bouwens et al. 2003b, 2004b, 2005a; Stanway et al. 2003; Yan & Windhorst 2004; Dickinson et al. 2004). There is a significant but modest decrease in the star formation rate from  $z \sim 2$  out to  $z \sim 6$  (Giavalisco et al. 2004a; Bouwens et al. 2005b). Studies of galaxy sizes indicate that high-redshift galaxies are compact in size ( $\sim 0.1'' - 0.3''$ ), while large ( $\gtrsim 0.4''$ ) low surface brightness galaxies are rare (Bouwens et al. 2004a). Furthermore, there is a clear decrease in size with redshift for objects of fixed luminosity, with a preferred redshift size scaling  $(1 + z)^{-1.05 \pm 0.21}$  (Bouwens et al. 2004a,

<sup>5</sup>Royal Observatory Edinburgh, Blackford Hill, Edinburgh, EH9 3HJ, UK

<sup>6</sup>Institute of Astronomy, Madingley Road, Cambridge CB3 0HA, UK

<sup>7</sup>Department of Physics and Astronomy, The Johns Hopkins University, 3400 North Charles Street, Baltimore, MD 21218

<sup>8</sup>Inst. Astrofísica de Andalucía (CSIC), Camino Bajo de Huétor, 24, Granada 18008, Spain

<sup>9</sup>Max-Planck-Institut für Astronomie, Knigstuhl 17, D-69117, Heidelberg, Germany

<sup>10</sup>National Aeronautics and Space Administration, Washington, DC

see also Ferguson et al. (2004)). Morphological analysis of LBGs indicates that they often possess brighter nuclei and more disturbed profiles than local Hubble types degraded to the same image quality (e.g. Lotz et al. 2004). NICMOS imaging of the UDF in  $J_{110}$  and  $H_{160}$  suggest that luminous galaxies at  $z \sim 7 - 8$  exist with a total UV luminosity density that is still significant compared to  $z \sim 6$  (Bouwens et al. 2004c). This suggests that cosmic star formation is a continuous process with only gradual changes in the UV luminosity density since  $z \sim 6 - 7$ .

Despite these advances in the study of the evolution of the highest redshift galaxies, *galaxy clusters* have been studied out to only  $z = 1.4$  (Mullis et al. 2005). High redshift clusters are X-ray luminous due to virialised gas and galaxies moving within the cluster gravitational potential. These clusters contain populations of old and relatively massive galaxies, as well as younger star-forming galaxies (e.g. Dressler et al. 1999; van Dokkum et al. 2000; Goto et al. 2005). The scatter in the color-magnitude relation for cluster ellipticals at  $z \sim 1$  is virtually indistinguishable from that at low redshift, suggesting that some of the galaxy populations in these clusters are already remarkably old (e.g. Stanford et al. 1998; Blakeslee et al. 2003a; Wuyts et al. 2004; Holden et al. 2005). Postman et al. (2005) measured the morphology-density relation (MDR) in seven  $z \sim 1$  clusters that have been observed with the ACS. Evolution in the MDR appears to be primarily due to a deficit of S0 galaxies and an excess of Spiral/Irr galaxies relative to the local galaxy population, while the MDR for ellipticals exhibits no such significant evolution between  $z \sim 1$  and  $z = 0$ .

It has become clear that the rich clusters began forming at earlier epochs than hitherto believed, and their progenitors may be found at much earlier epochs. Finding and studying these progenitors may yield powerful tests for (semi-)analytical models and  $N$ -body simulations of structure formation. Although these models are relatively successful in reproducing large-scale galaxy clustering and galaxy luminosity functions, they still remain relatively untested on cluster-sized scales because of the absence of observed cluster progenitors beyond  $z \sim 1$ .

Several good candidates for galaxy overdensi-

ties, possibly ‘protoclusters’<sup>11</sup>, have been discovered at very high redshift (e.g. Pascarelle et al. (1996); Keel et al. (1999); Francis et al. (2001); Möller & Fynbo (2001); Steidel et al. (1998, 2005); Shimasaku et al. (2003); Ouchi et al. (2005b)). These structures have been found often as by-products of wide field surveys using broad or narrow band imaging. Overdensities have been found as by-products of wide field surveys with broad or narrow band imaging, but also through an established technique that is based on the hypothesis that luminous radio sources are amongst the most massive forming galaxies at high redshift (e.g. De Breuck et al. 2002; Dey et al. 1997; Pentericci et al. 2001; Villar-Martín et al. 2005) that may pinpoint the location of overdense regions. The association of distant, powerful radio galaxies with massive galaxy and cluster formation is mainly based on two observational clues. First, radio galaxies form a bright envelope in the  $K$ -band Hubble redshift diagram (De Breuck et al. 2002), suggesting that their host galaxies are the prime candidates for later brightest cluster galaxies (BCGs) that dominate the deep potential wells of clusters. Second, high redshift radio galaxies have companion galaxies, ranging from the red galaxy overdensities at  $1.5 < z < 2$  (e.g. Sánchez & González-Serrano 1999, 2002; Thompson et al. 2000; Hall et al. 2001; Best et al. 2003; Wold et al. 2003) to the large excesses of LAEs discovered through deep narrow-band imaging and spectroscopic follow-up with the Very Large Telescope (VLT) of the European Southern Observatory (e.g. Pentericci et al. 2000; Kurk et al. 2003; Venemans et al. 2002, 2004, 2005).

Building on the excesses of LAEs discovered in the vicinity of distant radio sources, we are performing a survey of candidate LBGs in such radio-selected protoclusters with ACS. In Miley et al. (2004) and Overzier et al. (2006) we reported on the detection of a significant population of LBGs around radio galaxies at  $z = 4.1$  (TN J1338–1942) and  $z = 5.2$  (TN J0924–2201). Here, we will present a detailed analysis of the ACS observations of protocluster TN J1338–1942 at  $z = 4.1$ ,

<sup>11</sup>The term *protocluster* is commonly used to describe galaxy overdensities at high redshift ( $z \gtrsim 2$ ) with mass estimates that are comparable to those of the virialized galaxy clusters, but without any evidence for a virialized intra-cluster medium.

augmented by ground-based observations with the VLT. This structure is amongst the handful of overdense regions so far discovered at  $z > 4$ , as evidenced by 37 LAEs that represent a surface overdensity of  $\sim 5$  compared to other fields (Rhoads et al. 2000; Dawson et al. 2004; Shimasaku et al. 2003). The FWHM of the distribution is  $625 \text{ km s}^{-1}$ ,  $\sim 4 \times$  narrower than the narrowband filter used. The mass overdensity as well as the velocity structure is consistent with the global properties of  $z \sim 4$  protoclusters derived from  $N$ -body simulations combined with semi-analytical modeling (De Lucia et al. 2004; Venemans 2005, but see Monaco et al. (2005)). The protocluster may possibly harbor several sub-mm sources as well (De Breuck et al. 2004). The radio galaxy itself is extremely bright in the rest-frame UV/optical and the sub-mm, suggesting the formation of a massive galaxy. It has a complex morphology which we have interpreted as arising from AGN feedback on the forming ISM and a massive starburst-driven wind (Zirm et al. 2005).

The main issues that we will attempt to address include the following. What can the observational properties tell us about the star formation histories and physical sizes of LAEs and LBGs? In particular we wish to study these properties in relation to the overdense environment that the TN1338 field is believed to be associated with, analogous to galaxy environmental dependencies that have been observed at lower redshifts and are predicted by models (e.g. Kauffmann et al. 2004; Postman et al. 2005; De Lucia et al. 2005). How do the clustering and mass overdensity of the TN1338 structure compare to the ‘field’, and what is the relation to lower redshift galaxy clusters? In Sect. 2 we will describe the observations, data reduction and methods. We present our sample of LBGs in Sect. 3, and describe the rest-frame UV and optical properties of LBGs and LAEs. In Sect. 4 we present the results of a nonparametric morphological analysis. In Sect. 5 we will present the evidence for a galaxy overdensity associated with TN J1338–1942 and investigate its clustering properties. We conclude with a summary of the main results and a discussion in Sect. 6. We use a cosmology in which  $H_0 = 72 \text{ km s}^{-1} \text{ Mpc}^{-1}$ ,  $\Omega_M = 0.27$ , and  $\Omega_\Lambda = 0.73$  (Spergel et al. 2003). In this Universe, the luminosity distance is  $37.1 \text{ Gpc}$  and the angular scale size is  $6.9 \text{ kpc arcsec}^{-1}$

at  $z = 4.1$ . The lookback time is 11.9 Gyr, corresponding to an epoch when the Universe was approximately 11% of its current age. All colors and magnitudes quoted in this paper are expressed in the  $AB$  system (Oke 1971).

## 2. Observations and data reduction

### 2.1. ACS imaging

We observed one field with the ACS around the radio galaxy TN J1338–1942 (henceforward ‘TN1338’). These observations were part of the ACS Guaranteed Time Observing high redshift cluster program. To search for candidate cluster members on the basis of a Lyman-break at the approximate wavelength of  $\text{Ly}\alpha$  redshifted to  $z = 4.1$ , we used the Wide Field Channel to obtain imaging through the broadband filters<sup>12</sup>  $g_{475}$ ,  $r_{625}$ ,  $i_{775}$ , and  $z_{850}$ . The total observing time of 18 orbits was split into 9400 s in each of  $g_{475}$  and  $r_{625}$ , and 11700 s in each of  $i_{775}$  and  $z_{850}$ . The filter transmission curves are indicated in Fig. 1. The  $r_{625}$ -band may include  $\text{Ly}\alpha$  if present.

Each orbit of observation time was split into two 1200 s exposures to facilitate the removal of cosmic rays. The data were reduced using the ACS pipeline science investigation software (*Apsis*; Blakeslee et al. 2003b). After initial processing of the raw data through CALACS at STScI (bias/dark subtraction and flat-fielding), the following processing was performed by *Apsis*: empirical determination of image offsets and rotations using a triangle matching algorithm, background subtraction, the rejection of cosmic rays and the geometric correction and combining of exposures through drizzling using the STSDAS Dither package. The final science images have a scale of  $0.05 \text{ pixel}^{-1}$ . The total field of view is  $11.7 \text{ arcmin}^2$ . The radio galaxy ( $\alpha_{J2000} = 13^h38^m30^s$ ,  $\delta_{J2000} = -19^\circ42'30''$ ) is located about  $1'$  away from the image centre. The field further includes 12 of the 37 spectroscopically confirmed LAEs (Venemans et al. 2002, 2006). The resultant color image of the field is shown in Fig. 2, with  $g_{475}$  in blue,  $r_{625}$  in green, and  $z_{850}$  in red. The radio galaxy clearly stands out as the sole ‘green’ object

<sup>12</sup>We use  $g_{475}$ ,  $r_{625}$ ,  $i_{775}$  and  $z_{850}$  to denote magnitudes in the HST/ACS passbands F475W, F625W, F775W and F850LP, respectively, or to denote the passbands themselves.

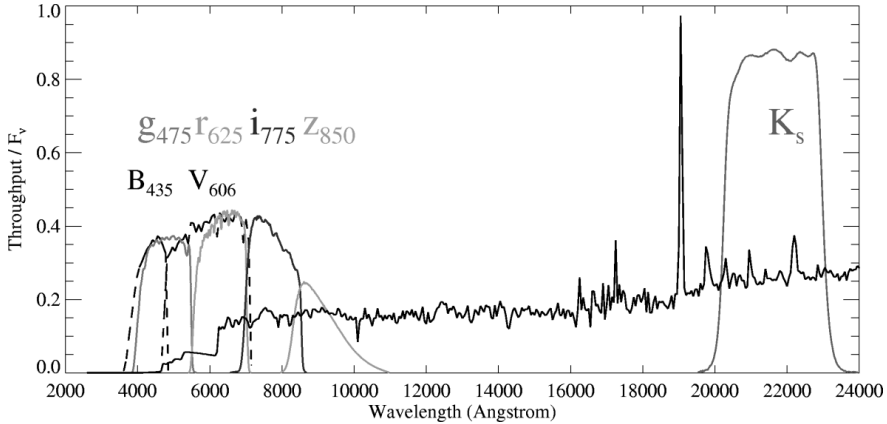


Fig. 1.— Total effective throughput of the HST/ACS  $g_{475}r_{625}i_{775}z_{850}$  and VLT/ISAAC  $K_S$  filters. The SED template shown is the *SB2* template from Benítez (2000) redshifted to  $z = 4.1$  following the attenuation prescription of Madau et al. (1996). The GOODS  $B_{435}V_{606}$  filters are indicated by dashed lines.

in the entire field, due to its prominent halo of Ly $\alpha$  emission observed in  $r_{625}$  (see Zirm et al. 2005).

We used the latest ACS zeropoints from Sirianni et al. (2005), and an extinction value of  $E(B - V) = 0.096$  from Schlegel et al. (1998). We measured the limiting magnitudes from the RMS of noise fluctuations in 10000 square apertures of varying size that were distributed over the images in regions free of objects. A summary of the observations and the limiting magnitudes are listed in Table 1.

## 2.2. VLT optical spectroscopy and NIR imaging

We obtained 10 hours of VLT/FORS2 spectroscopy in service mode<sup>13</sup>. The instrumental setup, the seeing conditions, and the method of processing of the data were similar as described in Venemans et al. (2002, 2005).

Near-infrared data in the  $K_S$ -band were obtained with VLT/ISAAC<sup>14</sup>. We observed a  $2.4' \times 2.4'$  field for 2.1 hours in March 2002, and for 5.4 hours in a partly overlapping field in 2004. After dark subtraction, flat fielding and rejection of science frames of poor quality, the data for each night was individually processed into a combined image using the XDIMSUM package in IRAF. Since only

the data taken on the night of March 26 2002 was considered photometric, the combined images of the other nights were scaled to match that particular night using several unsaturated stars for reference. We derived the zeropoint based on observations of the near-IR photometric standard FS 142. However, we had to adjust the zeropoint by 0.2 magnitudes to match the magnitudes of several 2MASS stars in the field. The seeing was  $\sim 0.5''$  (FWHM), and the galactic extinction in  $K_S$  was 0.036 mag.

Next, each of the combined images with the native ISAAC scale of  $0.148''/\text{pixel}$  was projected onto the  $0.05''/\text{pixel}$  ACS  $i_{775}$  image using the tasks GEOMAP/GEOTRAN in IRAF. Using  $\sim 25$  stars in common between the ACS image and the ISAAC images, the projection had a typical accuracy of 1.5 ACS pixels (RMS). Where available, reference stars close to the corners and edges of the images were selected so as to take out the effect of the geometric distortion on the ISAAC frames. The registered images were combined using a weighting based on the variance measured in a source-free region of each image. The limiting  $2\sigma$  depth in the AB<sup>15</sup> system was 25.2 magnitudes for a circular aperture of  $1.4''$  diameter. Areas that are only covered by either the 2002 or the 2004 data are shallower by 0.5 and 0.3 magnitudes, respectively. The  $K_S$ -band data cover 81% of the

<sup>13</sup>Program ID: 071.A-0495(A)

<sup>14</sup>Program ID: 073.A-0286(A)

<sup>15</sup> $K_{s,AB} = K_{s,Vega} + 1.86$

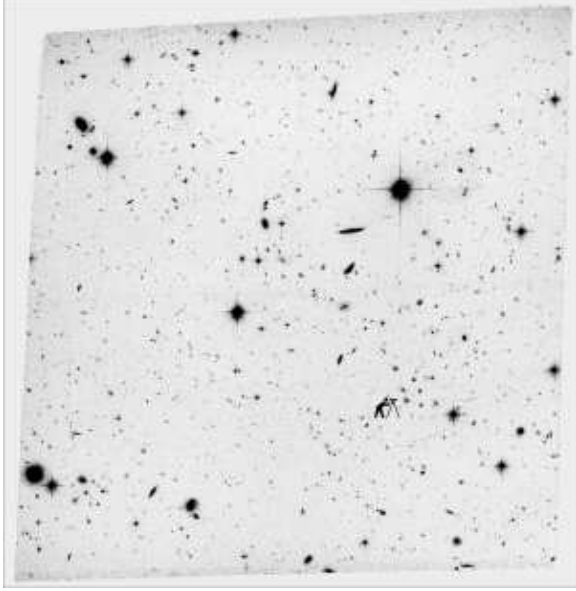


Fig. 2.— ACS color image showing  $g_{475}$  in blue,  $r_{625}$  in green and  $z_{850}$  in red. The field measures 11.7 arcmin $^2$ . The observer icon points at the location of the radio galaxy TN J1338–1942.

ACS field, and contain the radio galaxy and 11 LAEs.

### 2.3. Object detection and photometry

Object detection and photometry was done using the **SExtractor** software package of Bertin & Arnouts (1996). We used SExtractor in double-image mode, where object detection and aperture determination are carried out on the so-called “detection image”, and the photometry is carried out on the individual filter images. For the detection image we used an inverse variance weighted average of the  $r_{625}$ ,  $i_{775}$  and  $z_{850}$  images, and a map of the total exposure time per pixel was used as the detection weight map. Photometric errors were calculated using the root mean square (RMS) images from *Apsis*. These images contain the absolute error per pixel for each output science image. We detected objects by requiring a minimum of 5 connected pixels at a threshold of 1.5 times the local background ( $S/N$  of  $> 3.35$ ). The values for SExtractor’s deblending parameters (`DEBLEND_MINCONT = 0.1`, `DEBLEND_NTHRESH = 8`) were chosen to limit the

extent to which our often clumpy  $z \sim 4$   $g_{475}$ -dropouts were split into multiple objects. Our ‘raw’ detection catalog contained 3994 objects. We rejected all objects which had  $S/N$  less than 5 in  $z_{850}$ , where we define  $S/N$  as the ratio of counts in the isophotal aperture to the errors on the counts. The remaining 2022 objects were considered real objects, although they still contain a small fraction of artefacts.

We use SExtractor’s `MAG_AUTO` to estimate total object magnitudes within an aperture radius of  $2.5 \times r_{\text{Kron}}$  (Kron 1980). However, when accurate color estimation is more important than estimating a galaxy’s total flux, for example in the case of color-selection or when determining photometric redshifts, isophotal magnitudes are preferred because of the higher  $S/N$  and the smaller contribution of neighboring sources. Therefore we calculate *galaxy colors* from isophotal magnitudes. These procedures are optimal for (faint) object detection and aperture photometry with ACS (Benítez et al. 2004).

Optical-NIR (observed-frame) colors were derived from combining the ACS data with lower-resolution groundbased  $K_S$  data in the following way. We used `PSFMATCH` in *IRAF* to determine the 2D kernel that will match the point spread function in the ACS images to that obtained in the  $K_S$ -band, and convolved the ACS images with this kernel. The photometry was done using SExtractor in double image mode, using the  $K_S$ -band image for object detection. Colors involving the NIR data were determined in circular apertures with a diameter of 1''.4. For the radio galaxy TN J1338–1942 a circular aperture of 3''.0 diameter was used, due to its significantly larger size.

### 2.4. Aperture and completeness corrections

The photometric properties of galaxies are usually measured using source extraction algorithms such as SExtractor. We can conveniently use this software to determine aperture corrections and completeness limits as a function of e.g., the ‘intrinsic’ or real apparent magnitude, half-light radius ( $r_{hl}$ ) or the shape of the galaxy surface brightness profile (see also Benítez et al. 2004; Giavalisco et al. 2004b). To this end we populated the ACS  $z_{850}$  image with artificial galaxies consisting of a 50/50 mix of exponential and de Vaucouleurs pro-

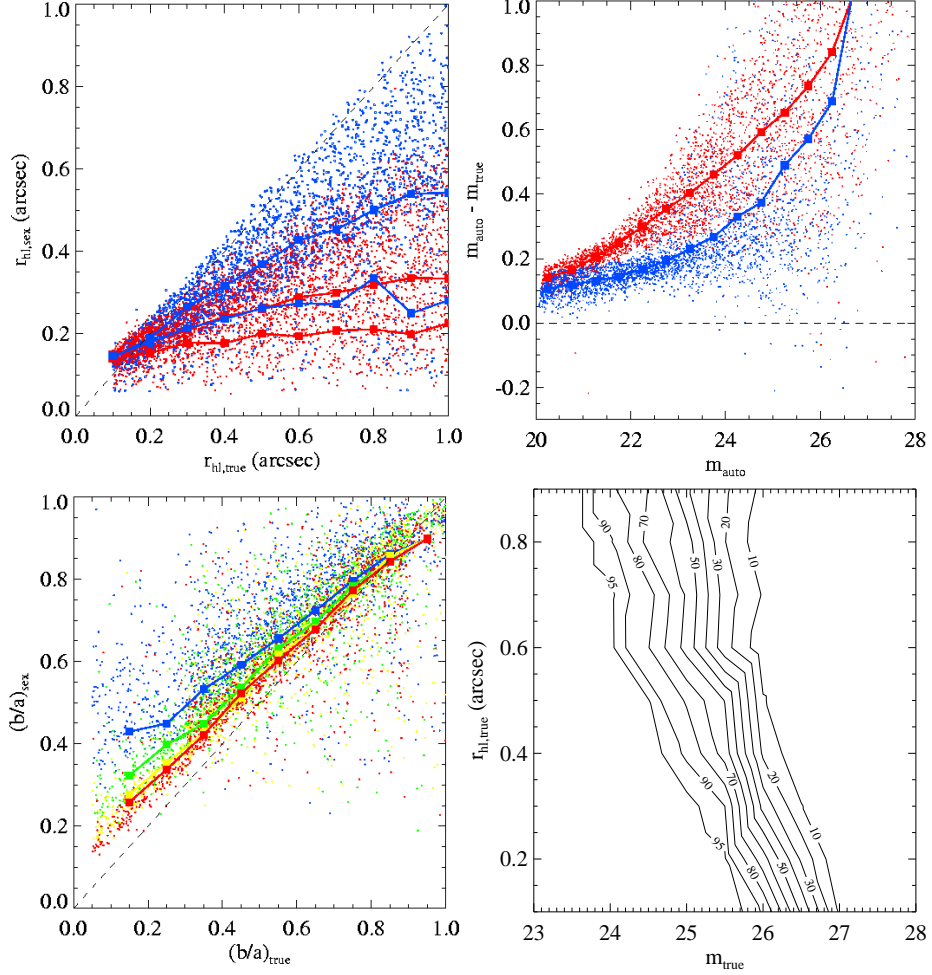


Fig. 3.— *Top left:* Intrinsic  $r_{hl,z}$  versus  $r_{hl,z}$  measured by SExtractor for de Vaucouleurs profiles (red points) and exponentials (blue points). The difference between intrinsic and measured radius is smaller for exponentials. The intrinsic sizes are increasingly underestimated when going to fainter magnitudes, e.g. from  $z_{850} \sim 24$  (blue/red upper lines) to  $z_{850} \sim 26$  (blue/red lower lines). — *Top right:* The difference between  $z_{850}$  MAG\_AUTO and total ‘intrinsic’ magnitudes for de Vaucouleurs profiles (red points) and exponentials (blue points). The median difference is indicated by the dashed line. — *Bottom left:* Input vs. recovered ellipticity  $(b/a)$  for sources with  $0''.1 < r_{hl} < 0''.3$  (blue),  $0''.3 < r_{hl} < 0''.5$  (green),  $0''.5 < r_{hl} < 0''.7$  (yellow), and  $0''.7 < r_{hl} < 0''.9$  (red). — *Bottom right:* Completeness limits in  $z_{850}$  as a function of total ‘intrinsic’ magnitudes and  $r_{hl}$ , where completeness is defined as the ratio of the number of objects detected to the number of artificial objects added to the image (50% exponential; 50% de Vaucouleurs). The 50% completeness limit lies at an intrinsic magnitude of  $\approx 26.5$  for small sources. When expressed in terms of the measured MAG\_AUTO magnitudes, the completeness limits shown here should be some  $\sim 0.5\text{--}1.0$  fainter, due to an underestimate of the ‘total’ fluxes for faint galaxies in our sample.

files. We simulated  $\sim 10,000$  galaxies with  $\sim 200$  per simulated image to avoid over-crowding. We took uniformly distributed half-light radii in the range  $0''.1$ – $1''.0$ , and uniformly distributed axial ratios in the range  $0.1$ – $1.0$ . Galaxies were placed on the images with random position angles on the sky. Using the zeropoint we scale the counts of each galaxy to uniformly populate the range  $z_{850}=20$ – $28$  magnitudes. We added Poisson noise to the simulated profiles, and convolved with the  $z_{850}$  point spread function (PSF). Next, SExtractor was used to recover the model galaxies as described in Sect. 2.3.

Approximately 75% of the artificial galaxies were detected. In Fig. 3 (top left) we show the measured  $r_{hl}$  versus the input ‘intrinsic’  $r_{hl}$ . Radii are increasingly underestimated as the input radii become larger, because the surface brightness gets fainter as  $r_{hl}^2$ . On average, the radius is underestimated by about 50% for a  $z_{850} \sim 26$  magnitude object with an intrinsic half-light radius of  $0''.4$ . The discrepancy between input and output radius is generally smaller for an exponential than for a de Vaucouleurs profile.

In Fig. 3 (top right) we show the aperture corrections defined by the difference between the SExtractor MAG\_AUTO magnitude and the total magnitude of the simulated profile. The amount of flux missed rises significantly towards fainter magnitudes, with a 0.5–1.0 magnitude correction for objects with output magnitudes of  $z_{850}=25$ – $27$ . For future reference, we also show the modeled versus the recovered ellipticities,  $b/a$ , in Fig. 3 (bottom left). The correspondence becomes poorer towards fainter and smaller objects, as well as more elongated ones. This is because the PSF causes small objects to appear generally rounder, and because the structural parameters are measured by SExtractor *after* convolving the image with a (Gaussian) detection kernel. Finally, in Fig. 3 (bottom right) we show the  $z_{850}$  completeness limits as a function of  $z_{850}$  and  $r_{hl}$ . About 50% completeness is reached at  $z_{850}=26$ – $26.5$  for unresolved or slightly resolved sources. Note that the 50% completeness limit will lie at measured MAG\_AUTO magnitudes that are fainter by 0.5–1.0 magnitude, given the significant aperture corrections presented in Fig. 3 (top right).

In the analysis that follows we will apply approximate corrections to the physical quantities

derived from measured  $r_{hl}$  and magnitudes (e.g. physical sizes, luminosities, and SFRs) based on the above results for exponential profiles. The quoted angular sizes and magnitudes are always as measured.

## 2.5. Photometric redshift technique

We will use the Bayesian Photometric Redshift code (BPZ) of Benítez (2000) to estimate galaxy redshifts,  $z_B$ . For a complete description of BPZ and the robustness of its results, we refer the reader to Benítez (2000) and Benítez et al. (2004). Our library of galaxy spectra is based on the elliptical, intermediate ( $Sbc$ ) and late type spiral ( $Scd$ ), and irregular templates of Coleman et al. (1980), augmented by two starburst galaxy templates with  $E(B-V) \sim 0.3$  ( $SB2$ ) and  $E(B-V) \sim 0.45$  ( $SB3$ ) from Kinney et al. (1996), and two simple stellar population (SSP) models with ages of 5 Myr and 25 Myr from Bruzual & Charlot (2003). The latter two templates have been found to improve the accuracy of BPZ for very blue, young high redshift galaxies in the UDF (Coe et al. 2005). BPZ makes use of a parameter ‘ODDS’ defined as  $P(|z-z_B| < \Delta z)$  that gives the total probability that the true redshift is within an uncertainty  $\Delta z$ . For the uncertainty we can take the empirical accuracy of BPZ for the HDF-N which has  $\sigma = 0.06(1+z_B)$ . For a Gaussian probability distribution a  $2\sigma$  confidence interval centered on  $z_B$  would get an ODDS of  $> 0.95$ . The empirical accuracy of BPZ is  $\sigma \approx 0.1(1+z_B)$  for objects with  $I_{814} \lesssim 24$  and  $z \lesssim 4$  observed in the  $B_{435}V_{606}I_{814}$ -bands with ACS to a depth comparable to our observations (Benítez et al. 2004). Note that we will be applying BPZ to generally fainter objects at  $z \sim 4$  observed in  $g_{475}r_{625}i_{775}z_{850}$ . The true accuracy for such a sample has yet to be determined empirically. The accuracy of BPZ may be improved by using certain *priors*. We apply the commonly used magnitude prior that is based on the magnitude distribution of galaxies in real observations (e.g. the HDF).

## 2.6. Template-based color-color selection of protocluster LBG candidates

We extracted LBGs from our catalogs using color criteria that are optimized for detecting star-forming galaxies at  $z \sim 4$  (Steidel et al. 1999; Ouchi et al. 2004a; Giavalisco et al. 2004a). To

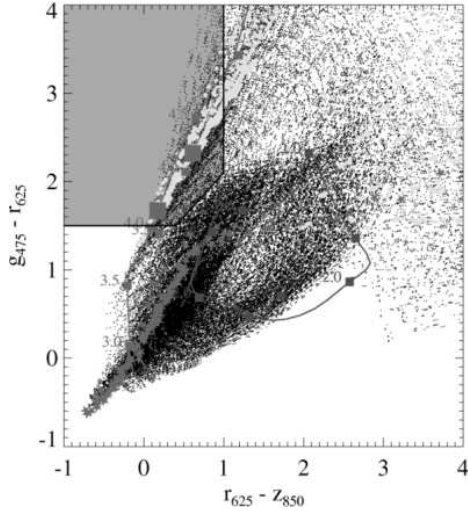


Fig. 4.—  $g_{475} - r_{625}$  versus  $r_{625} - z_{850}$  for model SEDs (points) simulated using the Bruzual & Charlot (2003) libraries. The model parameter grid is given in Table 2. Galaxies at  $z = 4.1$  are shown as (yellow) large solid circles. The shaded area is defined by  $g_{475} - r_{625} \geq 1.5$ ,  $g_{475} - r_{625} \geq r_{625} - z_{850} + 1.1$ ,  $r_{625} - z_{850} \leq 1.0$ . The spectral tracks are an elliptical (red solid line), an Sbc (red dashed line), an Scd (red dotted line), and a 100 Myr constant star formation model with  $E(B - V) = 0.0$  (blue solid line) and  $E(B - V) = 0.2$  (blue dotted line). Redshifts are indicated along the tracks. The redshift of the overdensity of Venemans et al. (2002) is marked by blue squares ( $z \approx 4.1$ ). Green stars mark the stellar locus based on the stellar SED library of Pickles (1998).

define the optimal selection for our filters we followed the approach employed by Madau et al. (1996). We used the evolutionary stellar population synthesis model code GALAXEV (Bruzual & Charlot 2003) to simulate a large variety of galaxy spectral energy distributions (SEDs) using: (i) the Padova 1994 simple stellar population model with a Salpeter (1955) IMF with lower and upper mass cutoffs  $m_L = 0.1 M_\odot$  and  $m_U = 100 M_\odot$  of three metallicities ( $0.2Z_\odot, 0.4Z_\odot, Z_\odot$ ), and (ii) the pre-defined star formation histories for instantaneous burst, exponentially declining ( $\tau = 0.01$  Gyr) and constant ( $t = 0.1, 1.0$  Gyr) star formation. We extracted spectra with ages between 1 Myr and 13 Gyr, applied the reddening law of Calzetti et al.

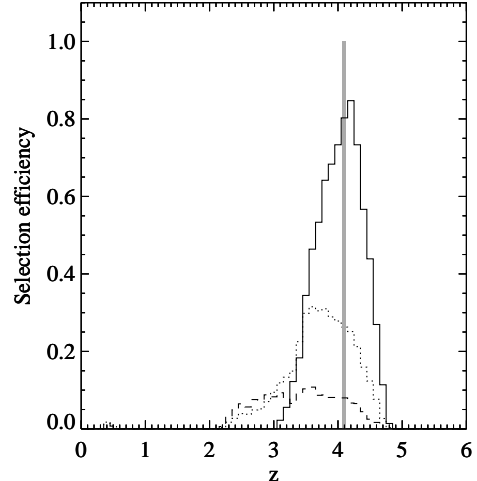


Fig. 5.— Selection efficiency for  $z \sim 4$  LBGs. The dotted histogram shows the fraction of model galaxies that meet the selection criteria in each redshift bin. The solid histogram shows the selection efficiency for model galaxies with ages less than 100 Myr and  $0 < E(B - V) < 0.3$ . The dashed histogram shows the fraction of models with ages greater than 0.5 Gyr selected, illustrating possible contamination of our  $z \sim 4.1$  sample by relatively old galaxies at  $z \sim 2.5$ . Another source of contamination is the inclusion of Balmer-break objects at  $z \sim 0.5$ . The shaded region indicates the redshift interval ( $z = 4.07 - 4.13$ ) of the protocluster of LAEs.

(2000) with  $E(B - V)$  of 0.0–0.5, and redshifted each spectrum to redshifts between 0.001 and 6.0, including the effects of attenuation by the IGM using the Madau et al. (1996) recipe. Galaxies were required to be younger than the age of the universe at their redshift, but other parameters were not tied to redshift. The full parameter grid is summarized in Table 2. While this approach is rather simplistic due to the fact that the model spectra are not directly tied to real observed spectra and luminosity functions, it is reasonable to expect that they at least span the range of allowed physical spectra. The resulting library can then be used to define a robust set of color criteria for selecting star-forming galaxies at the appropriate redshift, and estimating color-completeness

and contamination (Madau et al. 1996)<sup>16</sup>.

We extracted the model colors by folding each spectrum through the corresponding ACS filter transmission curves. No photometric scatter was applied to the models. The  $g_{475}-r_{625}$  and  $r_{625}-z_{850}$  color-color diagram is shown in Fig. 4. LBGs at  $z \sim 4$  can be isolated from lower redshift objects by a selection that is based on the  $g_{475}-r_{625}$  and  $r_{625}-z_{850}$  colors. For comparison, we have overplotted the color-color tracks of the standard spectral types from Benítez (2000). We elected to use the  $r_{625}-z_{850}$  color in defining our selection region (instead of the  $r_{625}-i_{775}$  color used in Miley et al. (2004)) due to the greater leverage in wavelength.

The color-color region that we use to select  $z \sim 4.1$  LBGs is defined as:

$$\begin{aligned} g_{475} - r_{625} &\geq 1.5, \\ g_{475} - r_{625} &\geq r_{625} - z_{850} + 1.1, \\ r_{625} - z_{850} &\leq 1.0. \end{aligned} \quad (1)$$

Fig. 5 shows the color selection efficiency as a function of redshift, defined as the number of galaxies selected in a redshift bin, divided by the total number of model galaxies in that redshift bin. The dotted histogram indicates the fraction of model galaxies meeting the selection criteria. The resulting redshift distribution has an approximately constant maximum efficiency of  $\sim 30\%$  for  $3.5 < z < 4.5$ . If we limit the model galaxies to ages less than 100 Myr and  $0 < E(B - V) < 0.3$  (consistent with the average LBG population at  $z \sim 3 - 4$  (Papovich et al. 2001; Steidel et al. 1999)), the color completeness (solid histogram) becomes  $\sim 90\%$  for models at  $z \sim 4.1$ . The dashed histogram shows the fraction of models with ages greater than 0.5 Gyr selected, illustrating the main sources of contamination in our  $z \sim 4.1$  sample, namely from relatively old galaxies at  $z \sim 2.5$  and the possible inclusion of Balmer-break objects at  $z \sim 0.5$ .

<sup>16</sup>Alternatively, these quantities can be estimated with more accuracy by carrying out extensive Monte Carlo simulations of model galaxies that follow the observed size and color distributions of dropout galaxies when observed with the typical photometric quality of the data (e.g. Steidel et al. 1999; Giavalisco et al. 2004a; Bouwens et al. 2005b). However, this requires samples that are significantly larger than our current sample for TN1338.

## 2.7. GOODS simulated images

To determine whether TN1338 is also host to an overdensity of LBGs at  $z \sim 4.1$ , we will want to compare the number of  $g_{475}$ -dropouts found in our ACS field with that found in a random field on the sky. Unfortunately, at present, there are not many ACS fields available, with comparable depths in  $g_{475}$ ,  $r_{625}$ , and  $z_{850}$  to carry out such comparison. We therefore avail ourselves of the four-band GOODS field for our control. The 3 orbit  $B_{435}$ , 2.5 orbit  $V_{606}$ , 2.5 orbit  $i_{775}$ , and 5 orbit  $z_{850}$  coverage is strikingly similar in depth and much larger in coverage, to the  $g_{475}r_{625}i_{775}z_{850}$  imaging we have on TN1338, suggesting that with simple wavelength interpolation, we should be able to mirror our TN1338 selection.

Though there are many ways to have performed this interpolation, we chose to perform the interpolation directly on the ACS data itself, changing it from the observed  $B_{435}V_{606}i_{775}z_{850}$  filter set to the  $g_{475}r_{625}i_{775}z_{850}$  filter set. This transformation was performed on a pixel-by-pixel basis, using the formula:

$$\begin{aligned} f_{i,j}^Y &= I_{i,j} g(SED, Y, i_{775}, z) + \\ &\Sigma_{X=X_L}^{X_H} \left( \frac{|\lambda(Y) - \lambda(X)|}{\lambda(X_H) - \lambda(X_L)} \right) \times \\ &g(SED, Y, X, z) \Delta f_{i,j}^X, \end{aligned} \quad (2)$$

$$(3)$$

where  $f_{i,j}^Y$  is the flux at pixel  $(i, j)$  in some band  $Y$ ,  $I_{i,j}$  is the best-fit fluxes in each pixel (expressed as an  $i_{775}$ -band flux),  $g(SED, Y, X, z)$  is a generalized  $k$ -correction from some band  $X$  to another band  $Y$  for some  $SED$  and redshift  $z$ ,  $\lambda(X)$  is the mean wavelength for some band  $X$ , the summation  $\Sigma_{X=X_L}^{X_H}$  runs over those bands which immediately straddle the  $Y$  band, and the  $\Delta f_{i,j}^X$  terms which account for the error in the fits to individual pixels. The best-fit fluxes  $I_{i,j}$  were determined by minimizing

$$\chi^2 = \Sigma_X \left[ \frac{I_{i,j} g(SED, X, i_{775}, z) - f_{i,j}^X}{\sigma_{i,j}^X} \right], \quad (4)$$

where  $f_{i,j}^X$  and  $\sigma_{i,j}^X$  are the flux and its uncertainty, respectively, in the  $X$  band at pixel position  $(i, j)$ . The error terms  $\Delta f_{i,j}^X$  are equal to  $f_{i,j} - g(SED, X, i_{775}, z)$ . The first term in Eq. 3 is a generalized  $k$ -correction applied to the best-fit model SEDs, while the second is an interpolation applied to the flux residuals from the fit. This is

nearly identical to expressions from Appendix B1 of Bouwens et al. (2003a) and represents a slight update to that procedure.

The redshifts  $z$  and SEDs  $SED$  we use for individual pixels are based upon an initial object catalog we made of each field before doing the transformation. Objects are detected off a  $\chi^2$  image (Szalay et al. 1999) constructed from the  $V_{606}i_{775}z_{850}$ -band using a fairly aggressive  $3\sigma$  threshold and splitting parameter (SExtractor DEBLEND\_MINCONT=0.005). Best-fit redshifts and SEDs are then estimated for each object from the photometry. These model parameters, in turn, are assigned to all the pixels which make up these objects (according to the SExtractor deblending maps), and thus used in the transformation given by Eq. 3. Only pixels belonging to objects with colors  $(B_{435} - V_{606}) > 0.8$ ,  $(B_{435} - V_{606}) > 0.6(V_{606} - z_{850}) + 0.5$ ,  $(B_{435} - V_{606}) > 3.375(V_{606} - z_{850}) - 4.575$  were transformed.

Since our ACS reduction of the TN1338 field had a different pixel scale (i.e.,  $0''.05$ ) than that of the GOODS v1.0 reduction ( $0''.03$ : Giavalisco et al. 2004b), we did not use that reduction as the basis for our simulation of the CDF-S GOODS field. Instead, we made use of an independent reduction we had made of the GOODS field with *Apsis*. That reduction was performed on a  $0''.05$  grid, using a procedure nearly identical to that described in Bouwens et al. (2005b), but using a ‘Lanzcos3’ kernel (which matches the TN1338 ACS reduction).

### 3. Properties of LBGs and LAEs in TN1338

We will apply the color-color section defined in the previous section to the TN1338 field to select a sample of candidate  $z \sim 4.1$  LBGs ( $g_{475}$ -dropouts) and study their properties in Sect. 3.1. In Sect. 3.2 we will study the same properties for the sample of  $z = 4.1$  LAEs within the ACS field. For completeness, new information obtained with ACS on a few low redshift MAMBO/VLA sources from the sample of De Breuck et al. (2004) is given in Appendix A.

#### 3.1. The $g_{475}$ -dropout sample

Using the selection criteria defined in Eq. 1 we extracted a sample of LBGs from the TN1338

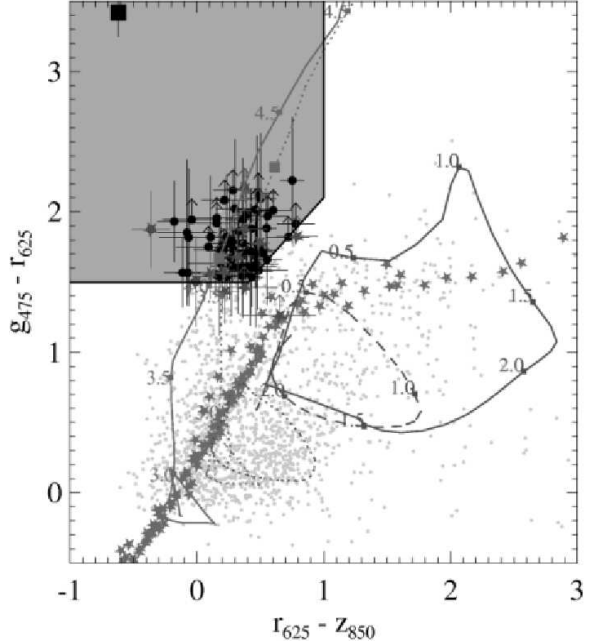


Fig. 6.— Color-color diagram of  $g_{475}$ -dropouts in TN1338 (circles) and the detection catalog (points). The shaded region shows our selection window (Eq. 1). Confirmed LAEs from Venemans et al. (2002) are marked by red stars, and the radio galaxy by the square. See the caption of Fig. 4 for further details.

field. In total there are 66 such objects in TN1338 with  $z_{850} < 27.0$ , 51 of which have  $z_{850} < 26.5$ , and 32 of which have  $z_{850} < 26.0$ . The color-color diagram is shown in Fig. 6. Although the stellar locus (based on Pickles (1998)) lies outside the region defined by our selection criteria, we required objects to have a SExtractor stellarity index of  $< 0.85$  (non-stellar objects with high confidence). This should exclude essentially all star-like objects from our sample.

##### 3.1.1. Star formation rates

The characteristic luminosity,  $L_{z=4}^*$ , of the LBG luminosity function at  $z \sim 4$  corresponds to  $z_{850} \sim 25.0$  (Steidel et al. 1999). The sample contains two objects, one of which is the radio galaxy, with a luminosity of  $\sim 6L^*$  ( $i_{775} \approx 23$ ). The remainder of the sample spans luminosities in the range  $\sim 0.4 - 2L^*$ , where we have applied aperture corrections

of up to  $\sim 1$  magnitude based on the exponential profiles in Fig. 3.

We calculated star formation rates (SFRs) from the emission-line free UV flux at 1500 Å ( $i_{775}$ ) using the conversion between luminosity and SFR for a Salpeter initial mass function (IMF) given in Madau et al. (1998):  $\text{SFR} (\text{M}_\odot \text{ yr}^{-1}) = L_{1500\text{\AA}} (\text{erg s}^{-1} \text{ Hz}^{-1})/8 \times 10^{27}$ . For ages that are larger than the average time that late-O/early-B stars spend on the main sequence, the UV luminosity is proportional to the SFR, relatively independent of the prior star formation history. The SFRs are listed in Table 4. The radio galaxy and object #367 each have a SFR of  $\sim 95 \text{ M}_\odot \text{ yr}^{-1}$ . The median SFR of the entire sample is  $\sim 8 \text{ M}_\odot \text{ yr}^{-1}$ . Although we assumed here that the LBGs are dust-free, one could multiply the SFRs by a factor of 2.5 to correct for an average LBG extinction of  $E(B - V) \approx 0.1$  (see next section) giving a median SFR of  $\sim 20 \text{ M}_\odot \text{ yr}^{-1}$ .

### 3.1.2. UV Continuum colors

We calculate the UV continuum slopes from the  $i_{775}-z_{850}$  color. This color spans the rest-frame wavelength range from  $\sim 1400$  Å to  $\sim 2000$  Å. We assume a standard power-law spectrum with slope  $\beta$  ( $f_\lambda \propto \lambda^\beta$ , so that a spectrum that is flat in  $f_\nu$  has  $\beta = -2$ ). We calculate

$$\beta_{iz} = \frac{\log_{10} \frac{Q_{850}}{Q_{775}} - 0.4(i_{775} - z_{850})}{\log_{10} \frac{\lambda_{775}}{\lambda_{850}}} - 2, \quad (5)$$

where  $\lambda_{775}$  and  $\lambda_{850}$  are the effective bandpass wavelengths, and  $Q_{775}$  and  $Q_{850}$  are the fractions of the continuum fluxes remaining after applying the recipe for foreground neutral hydrogen absorption of Madau (1995). The break at rest-frame 1216 Å only starts to enter the  $i_{775}$ -band for galaxies at  $z \gtrsim 4.7$ . Thus  $Q_{775}$  and  $Q_{850}$  are unity and  $\beta$  will be relatively independent of redshift for  $3.5 \lesssim z \lesssim 4.5$ . The uncertainties on  $\beta_{iz}$  were obtained by propagating the individual errors on the measured magnitudes. The measured slopes are plotted in Fig. 7. Excluding the two brightest sources, we find  $\langle \beta_{iz} \rangle = -1.95$ . This is significantly bluer than that found by Papovich et al. (2001), although it is consistent at the bright magnitude end where the comparison with  $L^*$  galaxies is appropriate (thin dashed line).

We have modeled the dependencies of the slope on age and dust using an exponential star formation history ( $\tau = 10$  Myr) with  $0.2Z_\odot$  metallicity and a Salpeter IMF. For a constant  $E(B - V) \approx 0.0$  the range of slopes favours ages in the range 50–300 Myr. A high dust content ( $E(B - V) \approx 0.3$ ) is incompatible with the majority of the slopes observed. A linear fit to the data gave a slope-magnitude relation of  $\beta_{iz} = (-0.16 \pm 0.05)(z_{850} - 25) - 1.84$  (thick solid line), which remains virtually unchanged when we excluded the two brightest objects (thick dashed line). There could be a possible higher incompleteness towards faint, relatively red objects (e.g. Ouchi et al. 2004a). However, the effect is likely to be much smaller than the observed correlation as shown by simulations incorporating  $B_{435}$ -dropout selection in GOODS (Bouwens et al. 2005b). Our relation is in good agreement with that of  $B_{435}$ -dropouts in GOODS of  $-0.21 \pm 0.03 \text{ mag}^{-1}$  found by Bouwens et al. (2005b). The best-fit relation spans ages in the range 5–150 Myr for a constant  $E(B - V) \approx 0.1$ . A similar slope-magnitude relation is also observed in other works (Meurer et al. 1999; Ouchi et al. 2004a) and may imply a mass-extinction or a mass-metallicity relation rather than a relation with age (Bouwens et al. 2005b). Interpreting the slope-magnitude relation as a mass-extinction relation implies  $E(B - V) \approx 0.13$  at  $z_{850} \approx 23$  and  $E(B - V) \approx 0.0$  at  $z_{850} \approx 27$  for a fixed age of 70 Myr.

### 3.1.3. Rest-frame UV to optical colors

At  $z \sim 4.1$ , the filters  $i_{775}$ ,  $z_{850}$  and  $K_S$  probe the rest-frame at  $\sim 1500$  Å, 1800 Å and 4300 Å, respectively. We detected 13 of the  $g_{475}$ -dropouts in the  $K_S$ -band at  $> 2\sigma$ . In Fig. 8 we show the  $i_{775}-K_S$  versus  $i_{775}-z_{850}$  color diagram.  $i_{775}-K_S$  color is more sensitive to the effects of age and dust than  $i_{775}-z_{850}$ , due to its longer lever arm in wavelength. Comparing the colors to the best-fit LBG SED from Papovich et al. (2001) redshifted to  $z \sim 4$  shows that the observed colors are consistent with ages in the range 10–100 Myr, although there will be degeneracy with dust. Non-detections in the  $K_S$ -band suggests that more than 50% of the  $g_{475}$ -dropouts have ages less than 70 Myr, with a significant fraction less than 30 Myr. The radio galaxy is among the reddest objects, although it has large gradients in  $i_{775}-K_S$  among

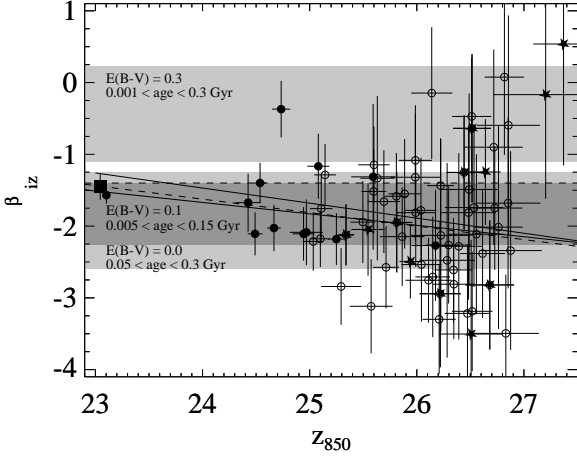


Fig. 7.—  $z_{850}$  versus  $\beta_{iz}$  for  $g_{475}$ -dropouts detected/undetected in  $K_S$  (filled/open circles), LAEs (stars), and the radio galaxy (square). The best-fit linear relations are indicated (thick lines, see text for details). The thin solid line is the relation for  $B_{435}$ -dropouts (Bouwens et al. 2005b). The best-fit SED from Papovich et al. (2001) redshifted to  $z = 4$  has  $\beta_{iz} \approx -1.4$  (thin dashed line). Shaded regions are for  $E(B - V) = 0.0$  with ages between 0.05 and 0.3 Gyr (bottom light shaded region),  $E(B - V) = 0.1$  with ages between 0.005 and 0.15 Gyr (dark shaded region), and  $E(B - V) = 0.3$  with ages between 0.001 and 0.3 Gyr (top light shaded region), assuming an exponential star formation history ( $\tau = 10$  Myr) with  $0.2Z_\odot$  metallicity and a Salpeter IMF.

its various stellar and AGN components (see Zirm et al. 2005). The age of  $\sim 100$  Myr was derived based on its average  $i_{775} - K_S$  color, it may actually consist of stellar components that are both significantly older and younger than 100 Myr, and does not rule out a significantly higher mass-weighted age for the galaxy as a whole.

In Fig. 9 we plot the  $i_{775} - K_S$  versus  $K_S$  color-magnitude diagram. Papovich et al. (2004) found evidence for a trend of generally redder colors for galaxies that are brighter in  $K_S$  in GOODS. The effect is not likely to be a selection effect because the objects are selected in the UV. Papovich et al. (2004) suggest that age and/or dust of LBGs at  $z \sim 3 - 4$  may increase with increasing rest-frame optical luminosity. Our data are consistent with

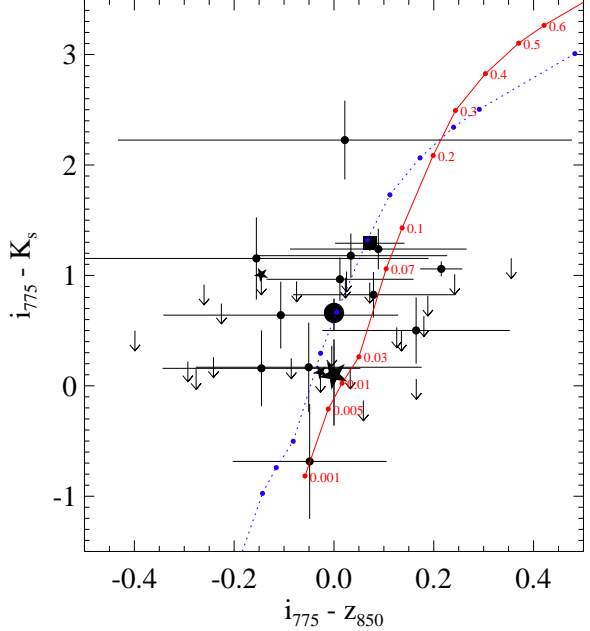


Fig. 8.— Rest-frame UV-optical colors of the  $g_{475}$ -dropouts (circles), the LAEs L9 and L25 (stars), and the radio galaxy (square). Arrows indicate  $2\sigma$  limits for non-detections in  $K_S$  (errors omitted for clarity). Lines indicate the colors of a  $\tau = 10$  Myr SED ( $0.2Z_\odot$ ) with ages in Gyr along the track for  $E(B - V) = 0.0$  (dotted) and  $E(B - V) = 0.15$  (solid). The large circle was obtained from a  $K_S$ -band stack of 12  $g_{475}$ -dropouts having  $25.3 < i_{775} < 26.4$ . The large star was obtained from a  $K_S$ -band stack of 5 LAEs within a similar magnitude range. Their  $i_{775} - K_S$  colors differ by  $\sim 0.7$  magnitude.

that conclusion.

### 3.1.4. Sizes

We measured  $r_{hl}$  in  $z_{850}$  using SExtractor by analysing the growth curve for each object out to  $2.5 \times r_{\text{Kron}}$ . Excluding the exceptionally large radio galaxy, the measured radii range from unresolved ( $\sim 0''.07$ ) to  $0''.42$ , corresponding to physical diameters of  $\lesssim 7$  kpc at  $z \sim 4$ . The average radius is  $0''.17$  or  $\sim 1.4$  kpc. If we divide our sample into two magnitude bins each containing an approximately equal number of objects (achieved by placing a cut at  $z_{850} = 26.1$  magnitude), the mean  $r_{hl}$  are  $0''.21 \pm 0''.01$  (error represents the standard de-

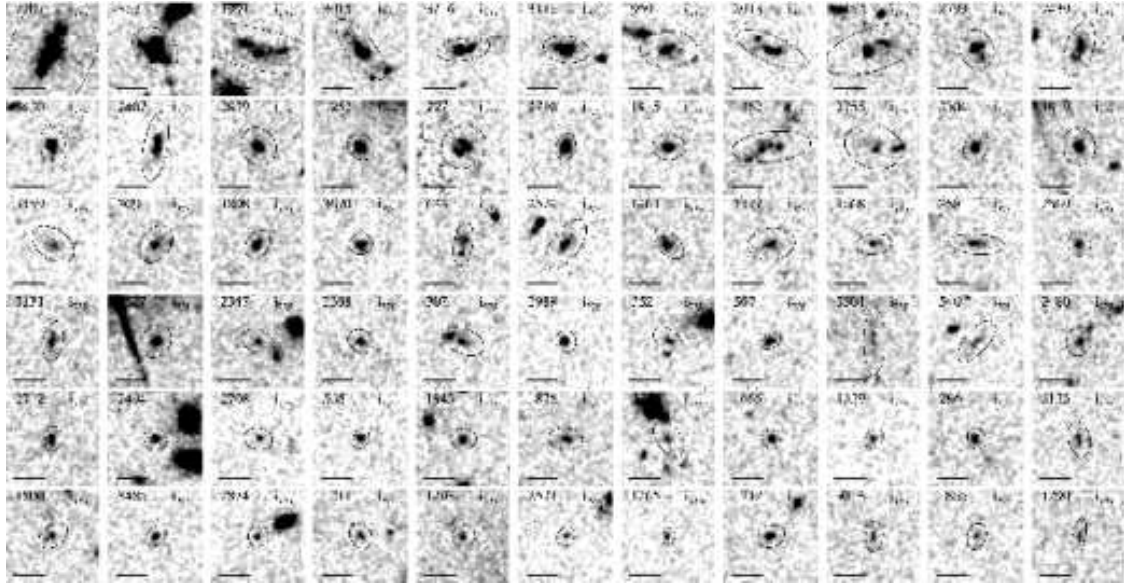


Fig. 10.—  $i_{775}$  postage stamps ( $3'' \times 3''$ ) of the  $g_{475}$ -dropout sample. The images have been smoothed using a Gaussian kernel of  $0''.075$  (FWHM). Kron apertures are indicated. The scale bars measure  $1''$ . North is up, East is to the left.

vation of the mean) and  $0.14 \pm 0.01$  in the bright and faint bins, respectively. The difference is expected to be largely due to a larger flux loss in the fainter sample (see Fig. 3), although fainter galaxies are also likely to be smaller because of the  $r_{200} \sim V_c \sim L^{1/3}$  luminosity-size relationship, where  $r_{200}$  is the virial radius and  $V_c$  is the circular dark matter halo velocity (see Mo et al. 1998).

The  $i_{775}$ -band morphologies of the  $g_{475}$ -dropouts are shown in Fig. 10. A separate section will be devoted to a nonparametric analysis of these morphologies and a comparison to field samples (see Sect. 4).

### 3.2. Ly $\alpha$ galaxies

Venemans et al. (2002) found an overdensity of LAEs ( $EW_{0,Ly\alpha} > 15\text{\AA}$ ), all spectroscopically confirmed to lie within  $625 \pm 150 \text{ km s}^{-1}$  of  $z = 4.11$ . All of the 12 LAEs in the ACS field have been detected in  $r_{625}$ ,  $i_{775}$  and  $z_{850}$  (see Table 3).

### 3.2.1. Star formation rates

The  $z_{850}$  magnitudes are in the range 25.3–27.4, corresponding to a luminosity range of  $\sim 0.2 - 1.0 L_*$ . The SFRs are  $\sim 1 - 14 M_\odot \text{ yr}^{-1}$  with

a median of  $5.1 M_{\odot} \text{ yr}^{-1}$  (not including the effect of dust). Venemans et al. (2005) calculated the SFRs from Ly $\alpha$  using  $\text{SFR} (M_{\odot} \text{ yr}^{-1}) = 8.7 L_{Ly\alpha} (\text{erg s}^{-1}) / 1.12 \times 10^{41}$ , from Kennicutt (1998) with the standard assumption of case B recombination (Brocklehurst 1971,  $L_{H\alpha} / L_{Ly\alpha} = 8.7$  for gas that is optically thick to HI resonance scattering and no dust). In general, we find good agreement between the SFRs calculated from the UV compared to Ly $\alpha$  with a median UV-to-Ly $\alpha$  SFR ratio of 1.3.

### 3.2.2. UV continuum colors

The UV slopes,  $\beta_{iz}$ , of the Ly $\alpha$  emitters are indicated in Fig. 7 (stars). The slope can be constrained relatively well for the four brightest emitters, which have  $-2.1 \pm 0.4$ ,  $-2.0 \pm 0.6$ ,  $-1.9 \pm 0.7$ , and  $-2.5 \pm 0.5$ . The LAE slopes scatter around the  $\beta_{iz}$ -magnitude relation for the  $g_{475}$ -dropouts found in Sect. 3.1.2, with a sample average of  $-1.7 \pm 1.2$ . These slopes are consistent with a flat (in  $f_\nu$ ) continuum, thereby favouring relatively low ages and little dust.

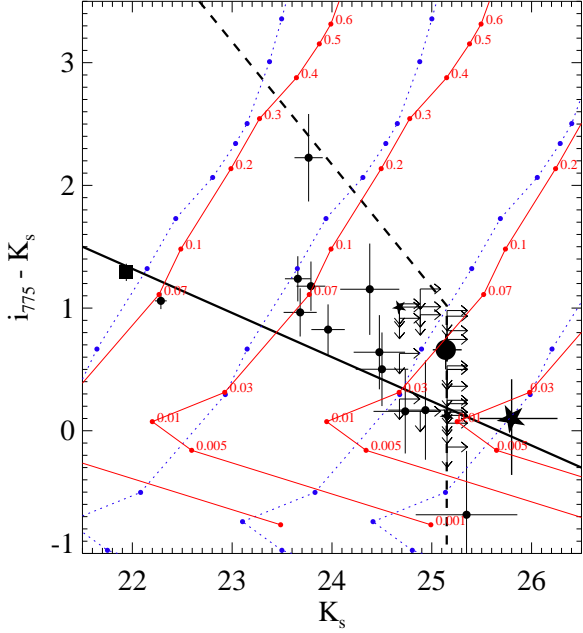


Fig. 9.— Color magnitude diagram of the  $g_{475}$ -dropouts (circles). The dashed line indicates the approximate  $2\sigma$  detection limits. The tracks are for  $\tau = 10$  Myr SEDs with different stellar masses (at  $t_{sf} = \infty$ ) of 0.03, 0.1, 0.5 and  $2 \times 10^{10} M_{\odot}$  for  $E(B - V) = 0.0$  (dotted) and  $E(B - V) = 0.15$  (solid). The thick solid line indicates the ‘blue envelope’ of Papovich et al. (2004), and suggests a color-magnitude relation in which luminosity correlates with either age or dust. See the caption of Fig. 8 for further details.

### 3.2.3. Rest-frame UV to optical colors

None of the 11 LAEs covered were detected in  $K_S$  at the  $> 2\sigma$  level. We created a stack of the  $K_S$ -band fluxes for the 5 LAEs that fell in the deepest part of our NIR image. The subsample had  $25.3 < z_{850} < 26.4$  and  $\langle (i_{775} - z_{850}) \rangle \approx 0.0$ . We obtained a  $3\sigma$  detection for the stack finding  $K_S = 25.8^{+0.46}_{-0.32}$  and hence  $i_{775} - K_S \approx 0.0$ . We compared this to a stack of 12  $g_{475}$ -dropouts with a similar range in  $z_{850}$  magnitudes and  $i_{775} - z_{850}$  colors, which gave a  $7\sigma$  detection with  $K_S = 25.14^{+0.16}_{-0.13}$  and  $i_{775} - K_S \approx 0.7$ . The results from the stacks have been indicated in Figs. 8 and 9. The difference in the  $i_{775} - K_S$  color is significant at  $\sim 2\sigma$ . A difference between the  $K_S$  luminosities of LBGs and LAEs is highly interesting given the very sim-

ilar UV magnitudes/colors of the two subsamples. A possible interpretation is discussed in Sect. 6.

### 3.2.4. Sizes and morphologies

We calculated  $r_{hl,r}$  from the  $r_{625}$ -band, the filter that includes Ly $\alpha$ , and compared it to the  $r_{hl}$  of the continuum calculated from the  $z_{850}$ -band (Table 3). The mean  $r_{hl}$  are  $0''.13$  in  $r_{625}$  and  $0''.12$  in  $z_{850}$ . At  $z = 4.1$ , the measured angular sizes correspond to physical radii of  $< 3$  kpc, with a mean value of  $\sim 1$  kpc. We do not find evidence for the sources to be more extended in  $r_{625}$  than they are in  $z_{850}$ , suggesting that Ly $\alpha$  emission is distributed in a very similar way to the continuum. One exception is source L7 which has  $r_{hl,r} = 0''.18$  compared to  $r_{hl,i} = 0''.13$  and  $r_{hl,z} = 0''.11$ .

We have measured the  $r_{hl}$  from a sample of 17 field stars in a similar magnitude range. The stars were selected on the basis of SExtractor stellarity index of 1.0. Four of the LAEs (L4, L11, L20, L22) have a  $r_{hl}$  in both bands that is indistinguishable from that of the stars. The UV luminosities of these unresolved LAEs are no different than those of the resolved ones. It is therefore unlikely that they contain an AGN nucleus that significantly overwhelms the host galaxy, making it appear unresolved. The light is probably due to unresolved stellar regions with  $r_{hl} \lesssim 500$  pc. If we restrict ourselves to resolved sources only, the mean  $r_{hl}$  are  $0''.15$  in both  $r_{625}$  and  $z_{850}$ .

The morphologies at rest-frame  $\sim 1500\text{\AA}$  are shown in Fig. 11 (see also Miley et al. (2004)). Two sources (L16 & L25) have double nuclei separated by  $\sim 0''.5$  ( $\sim 3$  kpc) that are connected by faint, diffuse emission. This is suggestive of merging systems.

## 4. Morphological analysis

In order to quantify the wide range in ACS continuum morphologies as observed in Fig. 10, we have carried out a nonparametric morphological analysis of the  $g_{475}$ -dropout sample. Following Lotz et al. (2004) we determined the following morphological coefficients. 1) The Gini coefficient ( $G$ ), a statistic for the relative distribution of an object’s flux over its associated pixels, 2)  $M_{20}$ , the normalised second order moment of the brightest 20% of a galaxy’s pixels, and 3) concentration ( $C$ ), the ratio of the circular radii containing 20% and

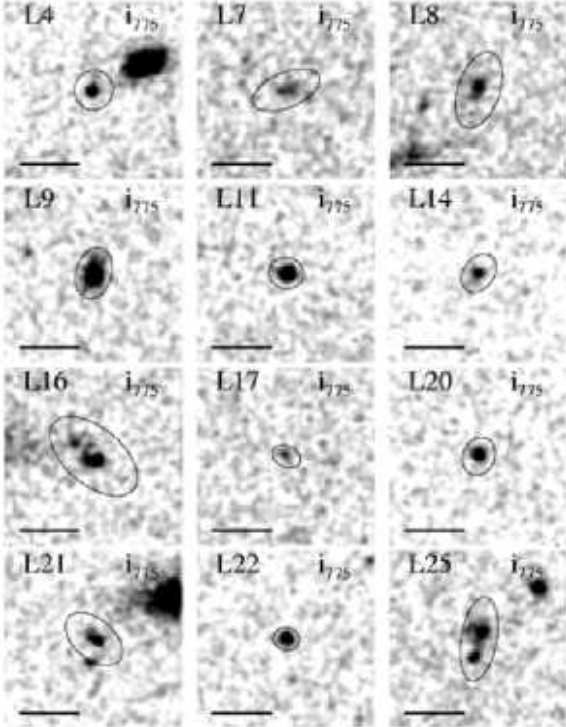


Fig. 11.—  $i_{775}$  postage stamps ( $3'' \times 3''$ ) of the twelve spectroscopically confirmed Ly $\alpha$  emitters of Venemans et al. (2002). See the caption of Fig. 10 for details.

80% of the total flux (see Conselice 2003, and references therein). The formulae have been adopted from Lotz et al. (2004).

To improve the  $S/N$  of our sample we coadded the  $i_{775}$  and  $z_{850}$  images, giving a total exposure time of 23500 s. To further improve the  $S/N$  per pixel the images were binned using a  $2 \times 2$  binning scheme. Pixels were flagged as belonging to an object if they were inside one ‘Petrosian radius’ (Petrosian 1976). This ensures that the morphological analysis is relatively insensitive to varying surface brightness limits and  $S/N$  among different objects (Lotz et al. 2004). After some initial tests, we maximized the number of  $g_{475}$ -dropouts with sufficient ( $S/N$ )<sub>pixel</sub> by setting the free Petrosian parameter  $\eta$  to 0.3. We measured the morphologies for a total of 15 of the  $g_{475}$ -dropouts that had ( $S/N$ )<sub>pixel</sub>  $> 3$ , which included the radio galaxy. The coefficients were all determined within a maximum radius of  $1.5 \times r_p$ . We used SExtractor’s segmentation maps to mask out all pixels suspected of belonging to unrelated sources. Errors on the coefficients were determined using Monte Carlo simulations. The value of each pixel was modified in such a way that the distribution of values were normally distributed with a standard deviation equal to that given by the RMS image value for the corresponding pixel.

In Fig. 12 we plot the distributions of the morphological parameters derived for the TN1338  $g_{475}$ -dropouts (blue points). The radio galaxy (large circle) has non-average values in each of the parameter spaces, owing to its complex morphology as described by Zirm et al. (2005). To compare the morphologies of the  $g_{475}$ -dropouts in TN1338 we have applied the morphological analysis also to a sample of  $z \sim 4$  LBGs selected in our GOODS CDF-S simulations (see Sect. 2.7). However, the morphological parameters were measured in the original, stacked  $i_{775}$  and  $z_{850}$  images from GOODS in case the morphologies were not preserved during the construction of the simulated images (Sect. 2.7). Fig. 12 indicates that both the centroids and the spread of the TN1338 parameter distributions (indicated with the blue contours) coincide with that of the parameter distributions determined from GOODS (red contours).

## 5. Evidence for an overdensity associated with TN J1338-1942 at $z = 4.1$ ?

### 5.1. Surface density distribution

In Fig. 13 we show the angular distribution of the  $g_{475}$ -dropouts in TN1338. Contours of the local object surface density compared to the average field surface density illustrate that the  $g_{475}$ -dropouts lie predominantly in a filamentary structure. Another density enhancement is located near the top edge of the image. Interestingly, both peaks in the object surface density distribution coincide with an extremely bright  $\sim 6L^*$  LBG. One of these is the radio galaxy, which takes a central position in the largest concentration of  $g_{475}$ -dropouts in the field. Moreover, about half of the dropouts lie in a  $2'1 \times 2'1$  region that includes the radio galaxy.

The subsample of  $g_{475}$ -dropouts detected in  $K_S$  are located only in the high density regions, most notably in the clump to the left of the radio galaxy. The objects detected in  $K_S$  are also the bright-

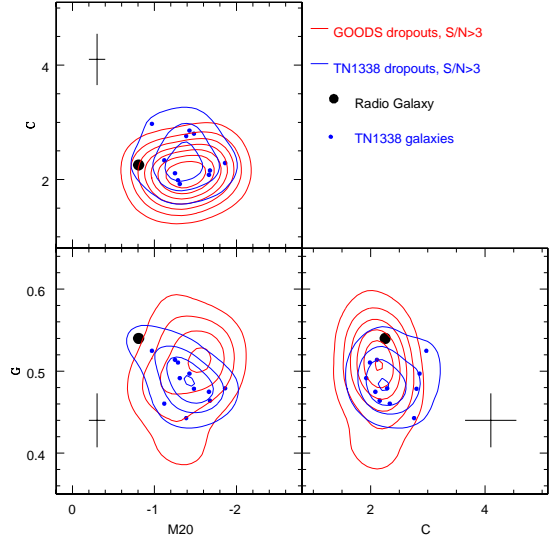


Fig. 12.— The morphological Gini coefficient (G),  $M_{20}$ , and concentration (C) for  $g_{475}$ -dropouts in TN1338 (blue points and contours), and  $g_{475}$ -dropouts in GOODS (red contours). The radio galaxy is indicated by the large circle. The approximate size of the error bars on the measurements are indicated.

est objects in the rest-frame UV. The filamentary distribution of the dropouts is not reflected by the angular distribution of the 12 LAEs, which are distributed more uniformly over the field. In fact, 8 of the emitters lie in regions that are underdense compared to the overall distribution of  $g_{475}$ -dropouts.

## 5.2. Comparison with ‘field’ LBGs from GOODS

Here we will test whether the suggestive structure of  $g_{475}$ -dropouts in TN1338 represent an overdensity of star-forming galaxies associated with TN J1338–1942, similar to the overdensity of LAEs discovered by Venemans et al. (2002). To determine the ‘field’ surface density of  $g_{475}$ -dropouts we have extracted a control sample by applying our selection criteria to the simulated images based on  $B_{435}$ -dropouts in the GOODS CDF-S as described in §2.7. A mosaic of the GOODS CDF-S fields is shown in Fig. 14. Points indicate the filamentary nature of the angular dis-

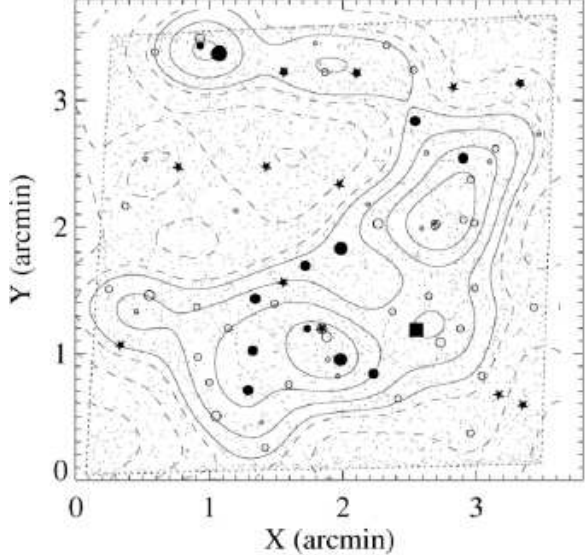


Fig. 13.— Object map of the  $g_{475}$ -dropout candidates (circles), TN J1338–1942 (square), Ly $\alpha$  emitters (stars) and the detection catalog (points).  $g_{475}$ -dropouts detected in  $K_S$  are indicated by filled circles. Larger circles indicate brighter objects in  $z_{850}$ . The contours represent density fluctuations  $\Delta \equiv (\Sigma - \bar{\Sigma})/\bar{\Sigma}$  of  $-1, -0.5, -0.1$  (dashed contours) and  $+0.1, +0.5, +1, +1.5$  (solid contours), achieved by smoothing the object map with a Gaussian of width  $36''$ , or 250 kpc (FWHM), using equal weights. LAEs that are not in the  $g_{475}$ -dropout sample were not included in the density contours.

tribution of LBGs at  $z \sim 4$ . At  $z_{850} < 27.0$  there are a total of 361  $g_{475}$ -dropouts in the transformed CDF-S in an area of 159 arcmin $^2$ , giving an average surface density of 2.27 arcmin $^{-2}$ , and 1.82 arcmin $^{-2}$ , and 1.16 arcmin $^{-2}$  for  $z_{850} < 26.5$  and  $z_{850} < 26.0$ , respectively. The surface density of  $g_{475}$ -dropouts in TN1338 is approximately 2.5× higher for each magnitude cut (5.64 arcmin $^{-2}$ , 4.36 arcmin $^{-2}$ , and 2.74 arcmin $^{-2}$ , respectively).

What is the significance of this factor 2.5 surface overdensity? LBGs belong to a galaxy population that is strongly clustered at every redshift (Porciani & Giavalisco 2002; Ouchi et al. 2004b), with non-negligible field-to-field variations. In our particular case, it is interesting to estimate the chance of finding a particular num-

ber of  $g_{475}$ -dropouts in a single  $3'4 \times 3'4$  ACS pointing. Analysing each of the 15 GOODS tiles individually, the lowest number of  $g_{475}$ -dropouts encountered was 12, and the highest was 37 to  $z_{850}=27.0$ . Next, we measured the number of objects in  $\sim 500$  randomly placed, square  $11 \text{ arcmin}^2$  cells in the GOODS mosaic shown in Fig. 14. The cells were allowed to overlap so that the chance of finding the richest pointing possible was 100%. In Fig. 15 (*top panel*) we show the histogram of counts-in-cells for the three different magnitude cuts. In each case the number of objects in TN1338 (indicated by the dashed lines) falls well beyond the high-end tail of the distribution, with none of the cells randomly drawn from GOODS containing as many objects (the highest being 41, 35, and 24 for  $z_{850}<27.0$ , 26.5, 26.0). Approximating the distributions with a Gaussian function (strictly spoken, this is only valid in the absence of higher order clustering moments, as well as non-linear clustering at very small scales), we find a surface overdensity of 2.5 at  $5 - 6\sigma$  significance with respect to the simulated GOODS CDF-S<sup>17</sup>. The measured standard deviations were corrected by 4% to take into account that the counts in cells distribution will appear narrower due to the fact that our control field is not infinitely large.

Comparable significance for an overdensity is found if we focus on a smaller region of  $4.4 \text{ arcmin}^2$ , where more than half of the  $g_{475}$ -dropouts are located (see Fig. 13). Drawing  $2'1 \times 2'1$  regions from the GOODS CDF-S field (Fig. 15, *bottom panel*) yielded a maximum of 21, 19 and 13 objects for the three magnitude cuts, respectively. The region in TN1338 corresponds to surface overdensities of 3.4, 3.2, and 4.0, but with  $\sim 5\sigma$  significance due to the fact that the counts-in-cells distribution function is much wider due to the relatively small cell size compared to the fluctuations in the surface density of LBGs

<sup>17</sup>We also selected a  $g_{475}$ -dropout sample on the basis of a SExtractor detection image that included the  $g_{475}$ -band image (as opposed to only  $r_{625}i_{775}z_{850}$ ). Due to the addition of mostly noise (for  $g_{475}$ -dropouts) this sample included less objects, and we found a surface overdensity of  $\sim 2$  at  $\gtrsim 3\sigma$ . This is slightly less significant, because the sample size in the simulations remained practically constant when selecting on  $g_{475}r_{625}i_{775}z_{850}$ . This suggests that the simulations may contain some extra crosstalk between filters as a result of the interpolation, and should be investigated a little further.

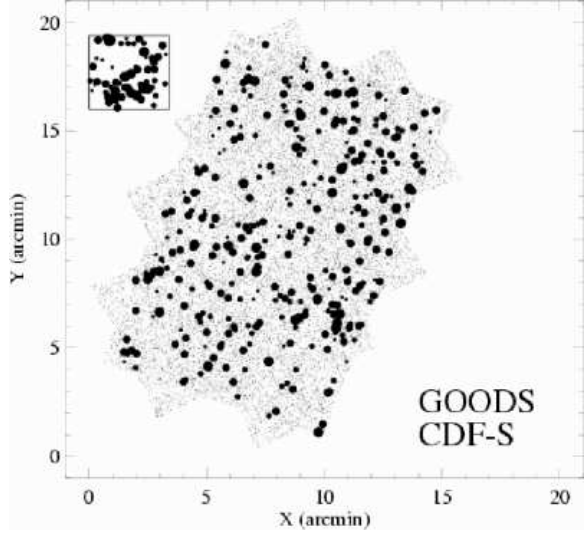


Fig. 14.— Distribution of  $z \sim 4$  LBGs in the GOODS CDF-S with  $z_{850} \leq 27.0$  (circles). Larger symbols correspond to brighter objects. The inset in the top left shows the  $3'4 \times 3'4$  TN1338 field and the distribution of  $g_{475}$ -dropouts at the same scale as the GOODS CDF-S for comparison.

(bottom panel).

We have not applied the counts in cells to simulations of the GOODS HDF-N, since it has been shown that the northern GOODS field is  $\sim 17\%$  less rich in  $B_{435}$ -dropouts compared to its southern counterpart (Bouwens et al. 2005b). We conclude that the number of  $g_{475}$ -dropouts in TN1338 represents a highly significant overdensity with respect to the  $314 \text{ arcmin}^2$  GOODS fields. Below we will further investigate implications of large-scale structure and cosmic variance.

### 5.3. $w(\theta)$ and sub-halo clustering

The two-point correlation function is one of the most powerful tools to study the large-scale distribution of high redshift galaxies. Recent measurements of the clustering of LBGs at  $3 < z < 5$  show that the angular correlation function,  $w(\theta)$ , deviates from the classical power-law at small angular scales. This behaviour is expected in the regime where non-linear clustering within single halos dominates over the large-scale clustering between halos. This effect has now been shown to be present (at least in a statistical sense) in large

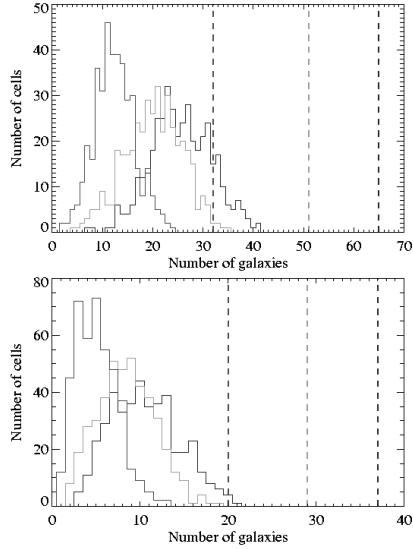


Fig. 15.— Counts in cells analysis of  $z \sim 4$  LBGs in the GOODS simulations compared to TN1338. *Top panel:* Histograms of the number of objects in square cells the size of TN1338 ( $3.4' \times 3.4'$ ) for  $z_{850} < 27.0$  (blue), 26.5 (green) and 26.0 (red). The number of  $g_{475}$ -dropouts in TN1338 are indicated by the vertical lines of corresponding color. *Bottom panel:* Same as top, but for  $2.1' \times 2.1'$  cells. The number of  $g_{475}$ -dropouts in TN1338 exceeds the number encountered in GOODS for every limiting magnitude or field size.

LBG samples (Ouchi et al. 2005a; Lee et al. 2005), although the contribution from each individual halo is quite small due to the relatively small halo occupations of LBGs as well as projection effects.

The structure found in TN1338 provides a unique opportunity to test the contribution of the one-halo term to  $w(\theta)$  within a single, over-dense field. We measured  $w(\theta)$  using the estimator  $w(\theta) = [A_1 DD(\theta) - 2A_2 DR(\theta) + RR(\theta)]/RR(\theta)$  with  $A_1 = N_r(N_r - 1)/(N_g(N_g - 1))$  and  $A_2 = (N_r - 1)/2N_g$  (Landy & Szalay 1993). We used 25 random catalogs of 10000 sources each, and the  $1\sigma$  errors on  $w(\theta)$  were estimated from the standard deviation among 32 bootstrap samples of the original data (Ling et al. 1986)<sup>18</sup>. When the

<sup>18</sup>In our case, deriving unweighted bootstrap errors is expected to significantly overestimate the errors, since it does not take into account that each of the  $g_{475}$ -dropouts in

field size is relatively small, the average density of a clustered distribution is overestimated because the field where the clustering is being measured is also the field where the average density has to be estimated from. We therefore estimated the integral constraint (IC) for the ACS/WFC field,  $IC/A_w = \sum_i RR(\theta_i)\theta_i^{-\beta}/\sum_i RR(\theta_i) = 0.073$ , where we assumed a fixed slope of  $\beta = 0.6$ . The result is plotted in Fig. 16. We used bins of  $10''$ , but excluded the separations of  $\theta < 1''$ . Since we do not expect any signal in the large-scale, 2-halo clustering due to the finiteness of our sample, we have safely applied the IC to the datapoints using the large-scale clustering amplitude  $A_w \approx 0.6$  for B-dropouts in GOODS at  $z_{850} \lesssim 26.5$  measured by Lee et al. (2005). At  $\theta > 20''$   $w(\theta)$  is consistent with no clustering at all. At  $\theta < 20''$  the two datapoints lie above the large-scale clustering amplitude. The scale at which we find a positive signal agrees well with the expected location of an upturn in  $w(\theta)$  due to sub-halo clustering (Ouchi et al. 2005a; Lee et al. 2005).

To test the significance of possible sub-halo clustering in the field of TN1338, we constructed a mock field having large-scale clustering properties resembling those of LBGs at  $z \sim 4$ . We used the formalism of Soneira & Peebles (1978) to create an object distribution with a choice two-point angular correlation function. The procedure is as follows. First a random position is chosen. This forms the center of a pair of points that are placed with a random position angle and separation  $\theta_1$ . Each point forms the center for a new pair with separation  $\theta_2 = \theta_1/\lambda$  and random position angles. This process is repeated until  $L$  levels, each level contributing  $2^L$  points with separations  $\theta_1/\lambda^{L-1}$  to the ‘cluster’. Next, a new cluster center is randomly chosen in the field, and the cluster is again populated with a depth of  $L$  levels. This is repeated until the mock field contains  $N$  clusters. The resulting point distribution will have a power-law two-point angular correlation function with its slope determined by the choice of  $\lambda$ , and its smallest and largest angular scales determined by the point separations at the first and the last levels,

TN1338 was already selected to have a secure  $> 5\sigma$  detection. We therefore conservatively allowed only the 15 faintest objects in the sample to be randomly subsampled by the bootstrap resampling. The brighter sources were always retained in the bootstrap subsamples.

respectively. Because we need both many levels to get sufficient signal in  $w(\theta)$  at all angular scales, and many clusters to get sufficient coverage of the area, the method above produces far too many points at first. It is therefore common to introduce a parameter,  $f$ , which is the probability that each point makes it into the final sample when drawing a random subsample. We then calculate the number of clusters  $N$  necessary to match a particular surface density given this  $f$ . The amplitude of the angular correlation function,  $A_w$ , solely depends on the choice of  $f$ , since the clusters are randomly distributed with respect to each other. We iteratively created mock samples with different  $f$  and measured  $w(\theta)$  until the best-fit amplitude matched the amplitude of the correlation function that we wish to model (corrected for the IC). The size of the mock field was set to  $17' \times 17'$  with a surface density of  $\approx 5 \text{ arcmin}^{-2}$  to match the density found in TN1338. To model the result of Lee et al. (2005),  $w(\theta) \approx 0.6\theta^{-0.6}$ , we required an  $f$  of 0.001 (with  $\theta_1 = 8.3'$  and  $L = 13$ ). Having modeled the observed two-point statistics successfully, we extracted  $25 3.4' \times 3.4'$  ‘ACS’ fields from the mock sample and measured the mean  $w(\theta)$  and its standard deviation. The result is indicated in Fig. 16 (shaded region). The mean  $w(\theta)$  corresponds well to the large-scale clustering that was built into the much larger total mock field (solid line). For  $\theta < 10''$  there is a  $2\sigma$  discrepancy between the clustering observed in TN1338 and the expected clustering of a similarly sized mock field. It is likely that the sub-clustering in the TN1338 field is the result of galaxies that are physically interacting on scales that are smaller than the typical halo scale sizes (see Sect. 6.2.2).

#### 5.4. Spectroscopy and photometric redshifts

Excluding the radio galaxy, 6 of the LAEs confirmed by Venemans et al. (2002) are also in our photometrically selected LBG candidate sample. These high equivalent width Ly $\alpha$  LBGs lie in a narrow redshift interval ( $\Delta z \approx 0.03$ ) centered on the redshift of the radio galaxy. We further obtained spectroscopic redshifts for three of the candidate LBGs in our sample. The spectrum of the  $\sim 6L^*$  object #367 shows several absorption lines typical for LBGs at a redshift of  $3.830 \pm 0.002$  (Fig. 18). Object #3018 was found to have a

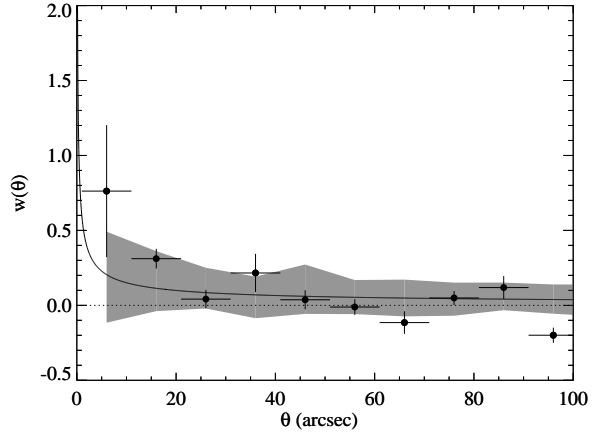


Fig. 16.— The angular two-point correlation function for  $g_{475}$ -dropouts in the TN1338 field. The solid line indicates the angular correlation function  $w(\theta) = 0.6\theta^{-0.6}$ , as measured for  $B_{435}$ -dropouts with  $z_{850} \lesssim 26.5$  in GOODS (Lee et al. 2005). The shaded region indicates the  $1\sigma$  spread in  $w(\theta)$  at each  $\theta$  that was measured among 25  $3.4' \times 3.4'$  fields of the same geometry and source density as the TN1338 field extracted from a  $17' \times 17'$  mock catalog with  $w(\theta) \approx 0.6\theta^{-0.6}$ .

redshift of  $z = 3.911 \pm 0.004$ , based on the presence of (faint) Ly $\alpha$  in emission, and OI/SiII  $\lambda 1303$  and CII  $\lambda 1334$  in absorption. Candidate #959 has strong Ly $\alpha$  (as confirmed by its asymmetry) at a redshift of  $z = 3.92 \pm 0.01$ . We also attempted to obtain a spectrum of object #3216. A very faint continuum was detected, but the  $S/N$  was insufficient to determine the redshift. Although the redshifts of these three LBGs in particular indicate no physical association with the radio galaxy and Ly $\alpha$  emitters, the spectroscopic results confirm that our  $g_{475}$ -dropout selection criteria successfully identify LBGs at  $z \approx 4$ .

We have computed the photometric redshifts of the  $g_{475}$ -dropouts in TN1338 and the ‘simulated’  $g_{475}$ -dropouts in GOODS. We let BPZ output the full redshift probability distribution for each object,  $P_i(z)$ , and summed over all the objects to get the total redshift probability distribution. In this manner, information about lower redshift likelihoods can be retained, and can the  $S/N$  of the overall photometric redshift distribution be improved because objects are not forced to only their

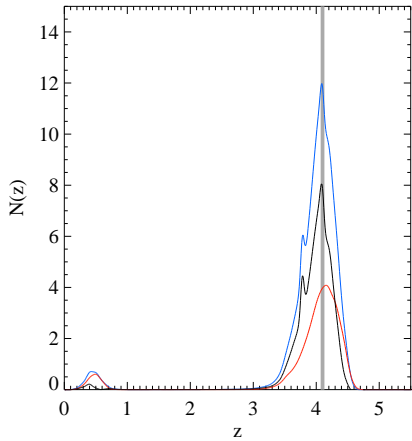


Fig. 17.— Total  $z_B$  probability distributions for  $g_{475}$ -dropouts in TN1338 (blue) and in GOODS CDF-S (red). The area under the blue curve is equal to the number of objects in the TN1338 sample. The red curve for GOODS has been normalised to the area of the TN1338 field. The GOODS curve was subtracted from the TN1338 curve to bring out the residuals of the redshift distribution for TN1338 (black curve). The residual  $z_B$  peak at the redshift of the radio galaxy and LAEs (shaded region). Another secondary peak lies at  $z_B \approx 3.8$ , the redshift of the other  $\sim 6L^*$  object in the field. The peak at  $z \sim 0.5$  are due to the alternative probability that a fraction of the  $g_{475}$ -dropouts could be 4000Å break objects.

best-fit value of  $z_B$ . The result is shown in Fig. 17. The area under the curves is equal to the total number of objects found in a 11.7 arcmin<sup>2</sup> area. According to BPZ the fraction of galaxies at  $z \sim 0.5$  totals  $\sim 4\%$  of the candidate  $z \sim 4$  sample in GOODS. The true contamination fraction is likely to be somewhat higher (Giavalisco et al. 2004a; Bouwens et al. 2005b). The difference in the areas under the two curves reflects the factor  $\sim 2.5$  overdensity of the TN1338 field. The peak of the  $z_B$  distribution lies at  $z = 4.1$ , which is a good match to the average redshift of the radio galaxy and the LAEs. The peak redshift for the  $g_{475}$ -dropouts from GOODS lies at a slightly higher redshift of  $z_B \approx 4.2$ . While the photometric redshift distribution of GOODS appears rather Gaussian,  $z_B$  is significantly steeper at  $z \approx 4.1$  for the  $g_{475}$ -dropouts in TN1338. The narrowness of

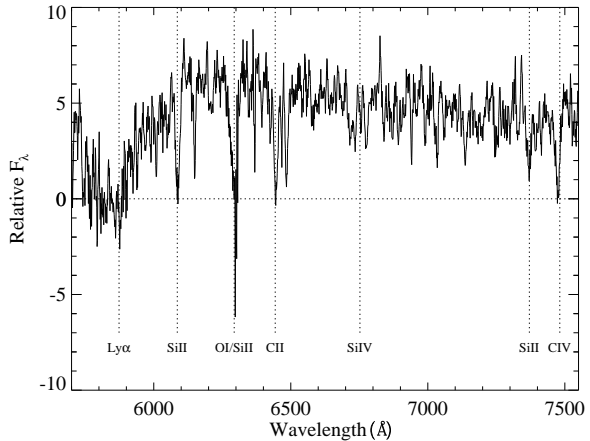


Fig. 18.— VLT/FORS2 spectrum of the Lyman break galaxy #367 with a redshift of  $3.830 \pm 0.002$ .

the distribution and the overdensity can be illustrated by subtracting the GOODS  $z_B$  distribution from that of TN1338 (black curve in Fig. 17). The photometric redshift distribution is further evidence that a significant fraction of these objects is likely to be physically related to the LAEs that are clustered around the radio galaxy.  $N(z)$  has a second peak around  $z \approx 3.8$ , although it contains much less objects. Interestingly, its redshift corresponds to the other  $\sim 6L^*$  object in the field.

## 6. Summary and Discussion

### 6.1. Properties of LBGs and LAEs

#### 6.1.1. SFRs, UV(-optical) colors, and masses

We studied the star forming properties of 66  $g_{475}$ -dropouts to  $z_{850} = 27$ , and 12 LAEs (6 of which were also in the  $g_{475}$ -dropout sample). The SFRs were in the range  $1\text{--}100 \text{ M}_\odot \text{ yr}^{-1}$ , with LAEs being limited to  $< 14 \text{ M}_\odot \text{ yr}^{-1}$ . Applying an average extinction ( $E(B-V) = 0.1$ ) yields SFRs of up to  $\sim 300 \text{ M}_\odot \text{ yr}^{-1}$ .

The LBGs and LAEs have very blue continua ( $\beta_{iz} \approx -2$ ) when averaged over the entire sample. We derived a UV-slope magnitude relation of  $\beta_{iz} = (-0.16 \pm 0.05)z_{850} + (2.16 \pm 1.26)$ , such that the slopes of  $L \gtrsim L^*$  LBGs are consistent with the average slopes determined for mildly redshifted LBGs at  $z \sim 3$  redshifted to  $z = 4$  (Papovich et al. 2001; Shapley et al. 2003, see also

Bouwens et al. (2005b)). The  $\beta_{iz} - z_{850}$  relation can be interpreted as a SFR- or mass-extinction relation implying  $E(B - V) \approx 0.13$  at  $z_{850} \approx 23$  and  $E(B - V) \approx 0.0$  at  $z_{850} \approx 27$  for a fixed age of  $\sim 70$  Myr.

We also derived rest-frame UV-optical colors, and estimated LBG ages in the range 10–100 Myr, with  $\sim 50\%$  of the LBGs having ages  $< 50$  Myr, with respect to our base template (exponentially declining,  $\tau = 10$  Myr,  $Z = 0.2Z_{\odot}$  and  $E(B - V) = 0.16$  from Papovich et al. 2001). We also found evidence for a relation in  $i_{775} - K_S$  vs.  $K_S$ , similar as found for  $B_{435}$ -dropouts in GOODS (Papovich et al. 2004). This is likely to be interpreted as a stellar mass-age and/or mass-dust relation, in the sense that the more massive galaxies have higher optical luminosities and redder UV-optical colors due to aging and/or dust.

None of the LAEs was detected in the  $K_S$ -band, but we found a  $3\sigma$  detection through stacking. The stacked magnitude of  $K_S = 25.8^{+0.44}_{-0.32}$  implied  $i_{775} - K_S \approx 0.0$ , while a stack of LBGs with similar UV magnitudes gave a  $7\sigma$  detection of  $K_S = 25.14^{+0.16}_{-0.13}$  and  $i_{775} - K_S \approx 0.7$ . Such a significant difference in the  $K_S$  magnitude while having similar  $i_{775}$  and  $i_{775} - z_{850}$  can only be explained if the LAEs are both younger as well as less massive than those LBGs (mass/age tracks have been indicated in Fig. 9). While it has been suggested before that Ly $\alpha$  emission can only escape during a relatively short, dust-less phase of star-formation, a mass difference would imply that the LAEs and LBGs are entirely different populations, at least in this field.

The observed range in  $K_S$ -band magnitudes in TN1338 of  $K_S \sim 26 - 22$  implies stellar masses (at  $t_{sf} = \infty$ ) ranging from  $\sim 3 \times 10^8$  for LAEs and the faintest LBGs to  $\sim 2 \times 10^{10} M_{\odot}$  for the radio galaxy and the brightest LBGs (Fig. 9).

To summarize, our “cluster” sample is in fair agreement with the rest-frame UV and UV-optical color-magnitude relations of field samples, suggesting that age (or dust) – while clearly correlated with the rest-frame UV/optical luminosity – is only weakly linked to environment.

#### 6.1.2. Sizes and morphologies

For  $L \geq L^*$  galaxies we found a mean half-light radius of  $0''.22$  ( $\sim 2$  kpc). Although this is

slightly smaller than the average size reported by Ferguson et al. (2004) based on a GOODS  $B_{435}$ -dropout sample, Ferguson et al. (2004) measured  $r_{hl}$  out to much larger circular annuli. The results are consistent when we apply a small aperture correction from Fig. 3. The mean  $r_{hl}$  of the  $g_{475}$ -dropouts is comparable to that of  $B_{435}$ -dropouts culled from the UDF and GOODS fields by Bouwens et al. (2004a), and is therefore consistent with the  $\propto (1 + z)^{-1.05 \pm 0.21}$  size scaling law that connects  $U_{300}$ - $B_{435}$ -,  $V_{606}$ -, and  $i_{775}$ -dropouts at fixed luminosities (Bouwens et al. 2004a). The  $r_{hl}$  of the  $L < L^*$  LAEs and LBGs are comparable ( $\sim 1.5$  kpc).

Our morphological classifications showed that the  $g_{475}$ -dropouts span a wide range of morphologies that are highly dissimilar to local Hubble types, but not dissimilar to  $B_{435}$ -dropouts in GOODS studied by Lotz et al. (2004, 2005).

We found no evidence for AGN among the LAEs, similar to a large field sample at  $z \sim 4.5$  studied by Wang et al. (2004). On the other hand, several of the LAEs in the protocluster near radio galaxy MRC 1138–262 at  $z = 2.16$  have been detected with *Chandra* indicating that the AGN fraction of such protoclusters could be significant (Pentericci et al. 2002; Croft et al. 2005). Upcoming Chandra observations of TN1338 will enable us to establish which of the LBGs/LAEs may harbor AGN.

## 6.2. Properties of the protocluster

### 6.2.1. Clustering segregation

We have presented evidence for an overdensity of  $g_{475}$ -dropouts in TN1338, and that this population has significant sub-clustering across the ACS field. The radio galaxy lies in a  $\sim 7.5$  (co-moving) Mpc ‘filament’ formed by the majority of the  $g_{475}$ -dropouts. The discovery of this substructure with ACS ties in closely with the clustering seen at larger scales. Intema et al. (2005) present the large-scale distribution of relatively bright  $B$ -dropouts towards TN1338 in a  $25' \times 25'$  field observed with the Subaru Telescope, showing several significant density enhancements amidst large voids.

In contrast, Venemans et al. (2002, 2005), using data from two  $7' \times 7'$  VLT/FORS fields, found that the LAEs are relatively randomly distributed.

Based on the absence of substructure and their small velocity dispersion they concluded that the LAEs might just be breaking away from the local Hubble flow. Additional evidence for this might be contained in the fact that the LAEs in the much smaller ACS field seem to prefer regions that are generally devoid of the UV-selected LBGs. We showed evidence that LAEs are generally younger (and possibly less massive) than objects in our UV-selected sample. Also,  $g_{475}$ -dropouts that were detected in  $K_S$  are both brighter and redder than LAEs, suggesting that objects with both higher ages or dust and larger stellar masses lie in the densest regions of the TN1338 field. This hints towards the formation of an age-density or mass-density relation in TN1338, analogous to the morphology-density relations or red-sequence relations observed at low redshift.

### 6.2.2. Halo sizes

We have compared the clustering of the  $g_{475}$ -dropouts to that expected based on the large-scale, two-halo contribution to  $w(\theta)$  measured for  $B_{435}$ -dropouts in clustered mock samples. We found an excess of clustering at the smallest angular scales ( $\theta < 20''$ ), which is expected when  $w(\theta)$  is dominated by non-linear sub-halo clustering at small scales (Ouchi et al. 2005a; Lee et al. 2005). These radii of  $\sim 0.3 - 0.6$  (co-moving) Mpc are similar to the virial radii,  $r_{200}$ , of dark matter halos with masses of  $10^{12-13} M_\odot$  (see Ouchi et al. 2005a), where  $r_{200}$  is defined as the radius of a sphere in which the mean density is  $200 \times$  the mean density of the Universe (Mo & White 2002). The linear bias,  $b$ , within these radii can reach values of  $> 10 - 50$ , compared to a bias of  $2.5 - 4$  for the field (Ouchi et al. 2005a; Lee et al. 2005). Together with the overdensity this explains the large number and sub-clustering of the  $g_{475}$ -dropouts in TN1338. The amplitude of the sub-halo correlation suggests that the occupation number of the proto-cluster “halo” is much higher than that of field halos on average, similar to what is expected from numerical simulations (e.g. Kravtsov et al. 2004).

TN1338 is further exceptional in the sense that it contains two  $\sim 6L^*$  LBGs, while there are only a few of such objects in the two GOODS fields combined. One is the radio galaxy at  $z = 4.11$ . The second object (#367) lies at a redshift of  $z = 3.83$ ,

and is also associated with a small enhancement in the  $g_{475}$ -dropout surface density. Possibly, the TN1338 field therefore contains not one, but *two* overlapping, large-scale structures at  $z \sim 4$ . Given their overall strong clustering properties and cosmic variance,  $z \sim 4$  LBGs will likely have significant field-to-field variations even on angular scales larger than currently probed by GOODS (Somerville et al. 2004). Future deep, wide surveys will demonstrate the uniqueness of protocluster structures such as found in the TN1338 field. Based on shallower samples, albeit of significantly larger areas, it has been found that the surface density of TN1338-like concentrations are comparable to that expected based on the co-moving volume densities of local clusters (e.g. Steidel et al. 1998; Shimasaku et al. 2003; Ouchi et al. 2005b; Intema et al. 2005). Observations of these kind of systems could constrain the halo occupation distribution at the very high mass end.

### 6.2.3. Mass of the overdensity

A proper determination of the mass of the TN1338 protocluster requires a good estimate of the total volume density, which depends on the actual redshift distribution of the LBGs and LAEs. We were not able to confirm any additional LBGs at the redshift of the radio galaxy. Not only due to the faintness of the targets, but also because all objects with high equivalent width Ly $\alpha$ , the most efficient method of confirming high redshift objects, had already been found previously. We nevertheless indirectly obtained redshifts of the 6  $g_{475}$ -dropouts that are also in the Ly $\alpha$  sample (excluding the radio galaxy). From the redshift distribution of LBGs in the GOODS simulations we expect 2.33 field LBGs at a redshift of  $z = 4.1$  with  $|z - \delta z| < 0.03$ . The volume overdensity in TN1338 is then  $\delta_g \equiv (\rho - \bar{\rho})/\bar{\rho} = 1.6$ , which can be considered to be a lower limit since it assumes that no other  $g_{475}$ -dropouts lie within  $\delta z$  of  $z = 4.1$ . Alternatively, given that only 20%–25% of field LBGs have high equivalent width Ly $\alpha$  to be detected as a LAE (Steidel et al. 2000), the 10 LAEs (with  $z_{850} < 27$ ) associated with TN1338 would represent 40–50 LBGs (including LAEs) in a relatively narrow redshift range. Note that if we subtract the average number of  $g_{475}$ -dropouts expected in a TN1338-sized field ( $\sim 26$ ) from the number of  $g_{475}$ -dropouts observed, the surplus in-

deed amounts to  $\sim 40$   $g_{475}$ -dropouts. This is independent confirmation of the results of Venemans et al. (2002) that were based on LAEs alone.

If we assume that the LBGs in TN1338 have the same overdensity as measured for the LAEs by Venemans et al. (2002), the overdensity in the TN1338 ACS field would be  $\delta_g \approx 3.5$ . We can relate the true mass overdensity,  $\delta_m$ , to the observed  $g_{475}$ -dropout overdensity,  $\delta_g$ , through  $1 + b\delta_m = |C|(1 + \delta_g)$ , where  $C = 1 + f - f(1 + \delta_m)^{1/3}$  (with  $f = \Omega_m(z)^{4/7}$ ) corrects for redshift-space distortion due to peculiar velocities assuming that the structure is just breaking away from the Hubble expansion (Steidel et al. 1998). Taking  $b \sim 3$  for  $B_{435}$ -dropouts with  $z_{850} < 26 - 27$  from Lee et al. (2005) gives  $\delta_m \sim 0.8$  for  $\delta_g = 3.5$ . This can be related to a total mass of  $M \simeq (1 + \delta_m)\bar{\rho}V \gtrsim 10^{14} M_\odot$ , where  $\bar{\rho}$  is the present-day mean density of the Universe and  $V$  is the volume probed by our ACS observations. The main uncertainty here is the total volume occupied by the mass overdensity, which could well span beyond the current ACS field (Venemans et al. 2002; Intema et al. 2005). The mass overdensity corresponds to a linear overdensity of  $\delta_L \sim 0.5$ , which when evolved to the present epoch corresponds to a linear overdensity of  $\delta_L \sim 2$  (see Steidel et al. 2005). This exceeds the linear collapse threshold of  $\delta_c = 1.69$ , so the structure will have virialized by  $z = 0$ . Taken together with the large estimate for its mass the term ‘protocluster’ is justified.

#### 6.2.4. Redshift evolution of the overdensity

In a subsequent paper, we will compare the number densities, masses, and total star formation rates of galaxies in protoclusters observed at a wide range of redshifts to the properties of massive clusters at  $z \lesssim 1$  extrapolated to the early Universe (Overzier et al., in prep.). The progenitors of galaxy clusters must have undergone rapid and intense star-formation (and possibly AGN activity) at  $z \gtrsim 2$ . The star formation in these ‘protoclusters’ is not only responsible for the buildup of the present-day stellar mass in cluster galaxies, but also for the chemical enrichment of the ICM (Ettori 2005). The ages of the stellar populations in massive red-sequence galaxies at  $z \sim 1$  are sufficiently high for them to be formed at redshifts  $2 < z < 6$  (e.g. Blakeslee et al. 2003b, Mei et al., In prep.). Simulations have indicated that

there are significant differences between the redshift of formation and redshift of assembly for the stellar mass in massive early-type galaxies: De Lucia et al. (2005) found that for elliptical galaxies with stellar mass larger than  $10^{11} M_\odot$  the median redshift at which 50% of the stars were formed is  $\sim 2.5$ , but the median redshift when those stars were actually assembled into a single galaxy lies only at  $\sim 0.8$ . In the same paper, they showed that the star formation properties of ellipticals depend strongly on the environment. For elliptical galaxies in clusters, the average ages can be up to 2 Gyr higher than those of similar mass ellipticals in the field. For an elliptical that is  $\sim 1$  Gyr older compared to the field, 50% of its stellar mass will already have been formed at  $z \sim 4$ . This stellar mass is likely to be formed in much smaller units, while the number of major mergers is considered to be relatively small (a few).

It is likely that the stellar mass formed by protocluster galaxies will end up in quiescent cluster early-types at lower redshifts, in accordance with the color-magnitude relation. However, there is a significant discrepancy between the masses of the LBGs and LAEs (both in protoclusters and in the field) and the masses of cluster ellipticals of  $\gtrsim 10$ . On the other hand, the number densities of LBGs found in e.g. TN1338 is a few times larger than the number of early-types on the red-sequence at  $z \sim 1$ , indicating that they can contribute still significant stellar mass through merging. Alternatively, protocluster fields may host other, older galaxies of significant mass, analogous to the population of distant red galaxies found at  $2 < z < 4$  (e.g. Franx et al. 2003; van Dokkum et al. 2003; Webb et al. 2005). These objects are believed to be the aged and reddened descendants of LBGs that were UV luminous only at  $z \gtrsim 5 - 6$ , and are therefore missed by the current object selection.

Recent numerical simulations of CDM growth predict that quasars at  $z \sim 6$  may lie in the center of very massive dark matter halos of  $\sim 4 \times 10^{12} M_\odot$  (Springel et al. 2005). They are surrounded by many fainter galaxies, that will evolve into massive clusters of  $\sim 4 \times 10^{15} M_\odot$  at  $z = 0$  (Springel et al. 2005). The discovery of galaxy clustering associated with luminous radio galaxies and quasars at  $z > 2$  is consistent with that scenario (e.g. Stiavelli et al. 2005; Overzier et al. 2006; Venemans et al. 2005, Zheng et al. 2005, this paper).

We thank Masami Ouchi for invaluable discussions and reading through the manuscript. We thank Ryan Quadri and Huib Intema for their contributions.

ACS was developed under NASA contract NAS 5-32865, and this research has been supported by NASA grant NAG5-7697 and by an equipment grant from Sun Microsystems, Inc. The Space Telescope Science Institute is operated by AURA Inc., under NASA contract NAS5-26555. We are grateful to K. Anderson, J. McCann, S. Busching, A. Framarini, S. Barkhouser, and T. Allen for their invaluable contributions to the ACS project at JHU.

## REFERENCES

Adelberger, K. L., Steidel, C. C., Giavalisco, M., Dickinson, M., Pettini, M., & Kellogg, M. 1998, *ApJ*, 505, 18

Barmby, P. et al. 2004, *ApJS*, 154, 97

Benítez, N. 2000, *ApJ*, 536, 571

Benítez, N. et al. 2004, *ApJS*, 150, 1

Bertin, E., & Arnouts, S. 1996, *A&AS*, 117, 393

Best, P. N., Lehnert, M. D., Miley, G. K., & Röttgering, H. J. A. 2003, *MNRAS*, 343, 1

Blakeslee, J. P., Anderson, K. R., Meurer, G. R., Benítez, N., & Magee, D. 2003a, in *ASP Conf. Ser. 295: Astronomical Data Analysis Software and Systems XII*, 257

Blakeslee, J. P., Anderson, K. R., Meurer, G. R., Benítez, N., & Magee, D. 2003b, in *ASP Conf. Ser. 295: Astronomical Data Analysis Software and Systems XII*, 257–+

Bouwens, R., Broadhurst, T., & Illingworth, G. 2003a, *ApJ*, 593, 640

Bouwens, R. J., Illingworth, G. D., Blakeslee, J. P., Broadhurst, T. J., & Franx, M. 2004a, *ApJ*, 611, L1

Bouwens, R. J., Illingworth, G. D., Blakeslee, J. P., & Franx, M. 2005a, Submitted to *ApJ*

Bouwens, R. J., Illingworth, G. D., Broadhurst, T. J., Meurer, G., Blakeslee, J. P., Franx, M., & Ford, H. 2005b, Submitted to *ApJ*

Bouwens, R. J. et al. 2003b, *ApJ*, 595, 589

—. 2004b, *ApJ*, 606, L25

—. 2004c, *ApJ*, 616, L79

Brocklehurst, M. 1971, *MNRAS*, 153, 471

Bruzual, G., & Charlot, S. 2003, *MNRAS*, 344, 1000

Cimatti, A., Andreani, P., Röttgering, H., & Tilanus, R. 1998, *Nature*, 392, 895

Coe, D., Benítez, N., Sanchez, S., Jee, M., Bouwens, R., & Ford, H. 2005, Submitted to *AJ*

Coleman, G. D., Wu, C.-C., & Weedman, D. W. 1980, *ApJS*, 43, 393

Conselice, C. J. 2003, *ApJS*, 147, 1

Croft, S., Kurk, J., van Breugel, W., Stanford, S. A., de Vries, W., Pentericci, L., & Röttgering, H. 2005, *AJ*, 130, 867

Daddi, E. et al. 2002, *A&A*, 384, L1

Dawson, S. et al. 2004, *ApJ*, 617, 707

De Breuck, C. et al. 2004, *A&A*, 424, 1

De Breuck, C., van Breugel, W., Stanford, S. A., Röttgering, H., Miley, G., & Stern, D. 2002, *AJ*, 123, 637

De Lucia, G., Kauffmann, G., Springel, V., White, S. D. M., Lanzoni, B., Stoehr, F., Tormen, G., & Yoshida, N. 2004, *MNRAS*, 348, 333

De Lucia, G., Springel, V., White, S., Croton, D., & Kauffmann, G. 2005, Accepted by *MNRAS*(astro-ph/0509725)

Dey, A., van Breugel, W., Vacca, W. D., & Antonucci, R. 1997, *ApJ*, 490, 698

Dickinson, M. et al. 2004, *ApJ*, 600, L99

Dressler, A., Smail, I., Poggianti, B. M., Butcher, H., Couch, W. J., Ellis, R. S., & Oemler, A. J. 1999, *ApJS*, 122, 51

Elston, R., Rieke, G. H., & Rieke, M. J. 1988, *ApJ*, 331, L77

Ettori, S. 2005, *MNRAS*, 362, 110

Ferguson, H. C. et al. 2004, *ApJ*, 600, L107

Ford, H. C. et al. 1998, in *Proc. SPIE Vol. 3356*, p. 234–248, *Space Telescopes and Instruments V*, Pierre Y. Bely; James B. Breckinridge; Eds., 234–248

Francis, P. J. et al. 2001, *ApJ*, 554, 1001

Franx, M. et al. 2003, *ApJ*, 587, L79

Giavalisco, M., & Dickinson, M. 2001, *ApJ*, 550, 177

Giavalisco, M. et al. 2004a, *ApJ*, 600, L103

—. 2004b, *ApJ*, 600, L93

Giavalisco, M., Steidel, C. C., Adelberger, K. L., Dickinson, M. E., Pettini, M., & Kellogg, M. 1998, *ApJ*, 503, 543

Goto, T. et al. 2005, *ApJ*, 621, 188

Hall, P. B. et al. 2001, *AJ*, 121, 1840

Holden, B. P. et al. 2005, *ApJ*, 620, L83

Intema, H., Venemans, B., Kurk, J., Ouchi, M., Kodama, T., Röttgering, H., Miley, G., & Overzier, R. 2005, Submitted to *A&A*

Kashikawa, N. et al. 2005, ArXiv Astrophysics e-prints

Kauffmann, G., White, S. D. M., Heckman, T. M., Ménard, B., Brinchmann, J., Charlot, S., Tremonti, C., & Brinkmann, J. 2004, *MNRAS*, 353, 713

Keel, W. C., Cohen, S. H., Windhorst, R. A., & Waddington, I. 1999, *AJ*, 118, 2547

Kennicutt, R. C. 1998, *ApJ*, 498, 541

Kinney, A. L., Calzetti, D., Bohlin, R. C., McQuade, K., Storchi-Bergmann, T., & Schmitt, H. R. 1996, *ApJ*, 467, 38

Kogut, A. et al. 2003, *ApJS*, 148, 161

Kravtsov, A. V., Berlind, A. A., Wechsler, R. H., Klypin, A. A., Gottlöber, S., Allgood, B., & Primack, J. R. 2004, *ApJ*, 609, 35

Kron, R. G. 1980, *ApJS*, 43, 305

Kurk, J., Röttgering, H., Pentericci, L., Miley, G., & Overzier, R. 2003, *New Astronomy Review*, 47, 339

Landy, S. D., & Szalay, A. S. 1993, *ApJ*, 412, 64

Lee, K., Giavalisco, M., Gnedin, O., Somerville, R., Ferguson, H., Dickinson, M. E., & Ouchi, M. 2005, Submitted to *ApJ*(astro-ph/0508090)

Ling, E. N., Barrow, J. D., & Frenk, C. S. 1986, *MNRAS*, 223, 21P

Lotz, J., Madau, P., Giavalisco, M., Primack, J., & Ferguson, H. 2005, *ApJIn Press* (astro-ph/0509106)

Lotz, J. M., Primack, J., & Madau, P. 2004, *AJ*, 128, 163

Möller, P., & Fynbo, J. U. 2001, *A&A*, 372, L57

Madau, P. 1995, *ApJ*, 441, 18

Madau, P., Ferguson, H. C., Dickinson, M. E., Giavalisco, M., Steidel, C. C., & Fruchter, A. 1996, *MNRAS*, 283, 1388

Madau, P., Pozzetti, L., & Dickinson, M. 1998, *ApJ*, 498, 106

McCarthy, P. J. et al. 2001, *ApJ*, 560, L131

Meurer, G. R., Heckman, T. M., & Calzetti, D. 1999, *ApJ*, 521, 64

Miley, G. K. et al. 2004, *Nature*, 427, 47

Mo, H. J., Mao, S., & White, S. D. M. 1998, *MNRAS*, 295, 319

Mo, H. J., & White, S. D. M. 2002, *MNRAS*, 336, 112

Monaco, P., Møller, P., Fynbo, J. P. U., Weidinger, M., Ledoux, C., & Theuns, T. 2005, *A&A*, 440, 799

Mullis, C. R., Rosati, P., Lamer, G., Böhringer, H., Schwope, A., Schuecker, P., & Fassbender, R. 2005, *ApJ*, 623, L85

Oke, J. B. 1971, *ApJ*, 170, 193

Ouchi, M. et al. 2005a, Submitted to *ApJ*(astro-ph/0508083)

—. 2005b, *ApJ*, 620, L1

—. 2004a, *ApJ*, 611, 660

—. 2004b, *ApJ*, 611, 685

Overzier, R. et al. 2006, *ApJ*, 637, 1

Papovich, C., Dickinson, M., & Ferguson, H. C. 2001, *ApJ*, 559, 620

Papovich, C. et al. 2004, *ApJ*, 600, L111

Pascarelle, S. M., Windhorst, R. A., Driver, S. P., Ostrander, E. J., & Keel, W. C. 1996, *ApJ*, 456, L21

Pentericci, L., Kurk, J. D., Carilli, C. L., Harris, D. E., Miley, G. K., & Röttgering, H. J. A. 2002, *A&A*, 396, 109

Pentericci, L. et al. 2000, *A&A*, 361, L25

Pentericci, L., McCarthy, P. J., Röttgering, H. J. A., Miley, G. K., van Breugel, W. J. M., & Fosbury, R. 2001, *ApJS*, 135, 63

Petrosian, V. 1976, *ApJ*, 209, L1

Pickles, A. J. 1998, *PASP*, 110, 863

Porciani, C., & Giavalisco, M. 2002, *ApJ*, 565, 24

Postman, M., ACS IDT, ACS IDT, ACS IDT, ACS IDT, ACS IDT, & ACS IDT. 2005, *ApJ*, Accepted for publication

Rhoads, J. E., Malhotra, S., Dey, A., Stern, D., Spinrad, H., & Jannuzi, B. T. 2000, *ApJ*, 545, L85

Sánchez, S. F., & González-Serrano, J. I. 1999, *A&A*, 352, 383

—. 2002, *A&A*, 396, 773

Schlegel, D. J., Finkbeiner, D. P., & Davis, M. 1998, *ApJ*, 500, 525

Shapley, A. E., Steidel, C. C., Pettini, M., & Adelberger, K. L. 2003, *ApJ*, 588, 65

Sheth, R. K., & Tormen, G. 1999, *MNRAS*, 308, 119

Shimasaku, K. et al. 2003, *ApJ*, 586, L111

Sirianni, M. et al. 2005, Submitted to *PASP*

Somerville, R. S., Lee, K., Ferguson, H. C., Gardner, J. P., Moustakas, L. A., & Giavalisco, M. 2004, *ApJ*, 600, L171

Soneira, R. M., & Peebles, P. J. E. 1978, *AJ*, 83, 845

Spergel, D. N. et al. 2003, *ApJS*, 148, 175

Springel, V. et al. 2005, *Nature*, 435, 629

Stanford, S. A., Eisenhardt, P. R., & Dickinson, M. 1998, *ApJ*, 492, 461

Stanway, E. R., Bunker, A. J., & McMahon, R. G. 2003, *MNRAS*, 342, 439

Steidel, C. C., Adelberger, K. L., Dickinson, M., Giavalisco, M., Pettini, M., & Kellogg, M. 1998, *ApJ*, 492, 428

Steidel, C. C., Adelberger, K. L., Giavalisco, M., Dickinson, M., & Pettini, M. 1999, *ApJ*, 519, 1

Steidel, C. C., Adelberger, K. L., Shapley, A. E., Erb, D. K. and Reddy, N. A., & Pettini, M. 2005, *ApJ* in Press (astro-ph/0502432), 626, 44

Steidel, C. C., Adelberger, K. L., Shapley, A. E., Pettini, M., Dickinson, M., & Giavalisco, M. 2000, *ApJ*, 532, 170

Steidel, C. C., Giavalisco, M., Pettini, M., Dickinson, M., & Adelberger, K. L. 1996, *ApJ*, 462, L17

Stiavelli, M. et al. 2005, *ApJ*, 622, L1

Szalay, A. S., Connolly, A. J., & Szokoly, G. P. 1999, *AJ*, 117, 68

Thompson, D., Aftreth, O., & Soifer, B. T. 2000, *AJ*, 120, 2331

van Dokkum, P. G. et al. 2003, *ApJ*, 587, L83

van Dokkum, P. G., Franx, M., Fabricant, D., Illingworth, G. D., & Kelson, D. D. 2000, *ApJ*, 541, 95

Venemans, B. 2005, Ph. D. Thesis, University of Leiden

Venemans, B. P. et al. 2002, *ApJ*, 569, L11

—. 2005, *A&A*, 431, 793

—. 2006, Accepted by A&A

—. 2004, A&A, 424, L17

Villar-Martín, M. et al. 2005, MNRAS, L112

Wang, J. X. et al. 2004, ApJ, 608, L21

Webb, T. et al. 2005, Accepted by ApJ(astro-ph/0511598)

Webb, T. M. et al. 2003, ApJ, 582, 6

Wold, M., Armus, L., Neugebauer, G., Jarrett, T. H., & Lehnert, M. D. 2003, AJ, 126, 1776

Wuyts, S., van Dokkum, P. G., Kelson, D. D., Franx, M., & Illingworth, G. D. 2004, ApJ, 605, 677

Yan, H., & Windhorst, R. A. 2004, ApJ, 612, L93

Zirm, A. W. et al. 2005, ApJ, 630, 68

TABLE 1  
SUMMARY OF OBSERVATIONS.

Filter	Date	$T_{exp}$ (s)	A (mag)	Depth (2 $\sigma$ )	Depth (5 $\sigma$ )
$g_{475}$ (F475W)	July 11–12 2002	9400	0.359	28.46 <sup>a</sup>	27.47 <sup>a</sup>
$r_{625}$ (F625W)	July 8–9 2002	9400	0.256	28.23 <sup>a</sup>	27.23 <sup>a</sup>
$i_{775}$ (F775W)	July 8–9 2002	11700	0.193	28.07 <sup>a</sup>	27.08 <sup>a</sup>
$z_{850}$ (F850LP)	July 11–12 2003	11800	0.141	27.73 <sup>a</sup>	26.73 <sup>a</sup>
$K_S$	2002, 2004	27000	0.036	25.15 <sup>b</sup>	24.16 <sup>b</sup>

<sup>a</sup>Measured in 0''.45 diameter square apertures.

<sup>b</sup>Measured in 1''.4 diameter circular apertures.

TABLE 2  
PARAMETER GRID OF SYNTHETIC SPECTRA.

SED Parameter	Values
Instantaneous burst	—
Exponential star formation timescales	0.01 Gyr
Constant star formation durations	0.1 1.0 Gyr
Ages	0.001 0.005 0.01 0.03 0.07 0.1 0.2 0.3 0.4 0.5 0.6 0.7 0.8 0.9 1.0 1.1 1.2 1.3 1.4 2.0 3.0 5.0 7.0 13.0 Gyr
Metallicities	0.2 $Z_{\odot}$ 0.4 $Z_{\odot}$ 1.0 $Z_{\odot}$
$E(B - V)$	0.0 0.1 0.2 0.3 0.4 0.5
Redshifts	0.001 0.01 0.05 0.1 0.15 0.2 0.25 0.3 0.35 0.4 0.45 0.5 0.55 0.6 0.65 0.7 0.75 0.8 0.85 0.9 0.95 1.0 1.1 1.2 1.3 1.4 1.5 1.6 1.7 1.8 1.9 2.0 2.1 2.2 2.3 2.4 2.5 2.6 2.7 2.8 2.9 3.0 3.1 3.2 3.3 3.4 3.5 3.6 3.7 3.8 3.9 4.0 4.1 4.2 4.3 4.4 4.5 4.6 4.7 4.8 4.9 5.0 5.1 5.2 5.3 5.4 5.5 5.6 5.7 5.8 5.9 6.0

TABLE 3  
PROPERTIES OF THE SPECTROSCOPICALLY CONFIRMED Ly $\alpha$  EMITTERS.

ID	$\alpha_{J2000}$	$\delta_{J2000}$	$z_{spec}$	$(g_{475} - r_{625})^a$	$(r_{625} - z_{850})^a$	$(i_{775} - z_{850})^a$	$z_{850}^b$	$r_{hl,r}$	$r_{hl,z}$	$SFR_{UV}^c$
RG	13:38:26.05	-19:42:30.47	4.105	$3.42 \pm 0.17$	$-0.61 \pm 0.03$	$0.09 \pm 0.03$	$23.05 \pm 0.05$	$0''.60$	$0''.62$	$93.7_{-0.59}^{+2.71}$
L4	13:38:22.46	-19:44:33.67	4.095	$1.88 \pm 0.27$	$-0.35 \pm 0.15$	$-0.14 \pm 0.16$	$26.68 \pm 0.23$	$0''.09$	$0''.08$	$4.83_{-0.53}^{+0.85}$
L7	13:38:24.78	-19:41:33.66	4.106	$> 1.26$	$0.65 \pm 0.29$	$0.32 \pm 0.25$	$27.20 \pm 0.49$	$0''.18$	$0''.11$	$3.22_{-0.67}^{+0.77}$
L8	13:38:24.86	-19:41:45.49	4.102	$> 1.47$	$0.37 \pm 0.27$	$-0.26 \pm 0.23$	$26.51 \pm 0.30$	$0''.12$	$0''.16$	$6.25_{-0.77}^{+0.88}$
L9	13:38:25.10	-19:43:10.77	4.100	$1.78 \pm 0.25$	$0.49 \pm 0.09$	$-0.02 \pm 0.07$	$25.34 \pm 0.08$	$0''.12$	$0''.14$	$14.4_{-0.58}^{+0.60}$
L11	13:38:26.16	-19:43:34.31	4.101	$1.56 \pm 0.18$	$0.11 \pm 0.09$	$-0.08 \pm 0.09$	$25.94 \pm 0.10$	$0''.08$	$0''.09$	$8.95_{-0.46}^{+0.48}$
L14	13:38:28.72	-19:44:36.98	4.102	$> 1.88$	$0.37 \pm 0.18$	$0.24 \pm 0.18$	$26.52 \pm 0.18$	$0''.13$	$0''.13$	$4.29_{-0.48}^{+0.54}$
L16	13:38:29.66	-19:43:59.82	4.102	$1.43 \pm 0.23$	$0.22 \pm 0.12$	$-0.00 \pm 0.11$	$25.54 \pm 0.16$	$0''.16$	$0''.19$	$11.4_{-0.00}^{+1.10}$
L17	13:38:29.86	-19:43:25.84	4.093	$> 1.57$	$0.21 \pm 0.27$	$0.44 \pm 0.29$	$27.37 \pm 0.28$	$0''.11$	$0''.10$	$1.33_{-0.31}^{+0.40}$
L20	13:38:32.83	-19:44:6.934	4.100	$> 2.17$	$0.37 \pm 0.15$	$0.13 \pm 0.14$	$26.44 \pm 0.16$	$0''.09$	$0''.11$	$5.12_{-0.48}^{+0.53}$
L21	13:38:33.56	-19:43:36.00	4.097	$1.50 \pm 0.32$	$-0.00 \pm 0.18$	$-0.16 \pm 0.18$	$26.22 \pm 0.19$	$0''.12$	$0''.18$	$4.75_{-0.79}^{+0.79}$
L22	13:38:34.14	-19:42:52.68	4.096	$> 1.82$	$0.79 \pm 0.16$	$0.13 \pm 0.13$	$26.64 \pm 0.14$	$0''.07$	$0''.08$	$4.69_{-0.38}^{+0.38}$
L25	13:38:34.96	-19:42:24.95	4.093	$1.68 \pm 0.33$	$0.32 \pm 0.13$	$0.00 \pm 0.12$	$25.81 \pm 0.15$	$0''.25$	$0''.24$	$9.94_{-0.72}^{+0.78}$

<sup>a</sup>Isophotal colors. The limits are 2 $\sigma$ .

<sup>b</sup>Total magnitudes.

<sup>c</sup>SFR estimated from the UV continuum flux ( $i_{775}$ ).

TABLE 4  
PROPERTIES OF THE  $z \sim 4$  LYMAN BREAK SAMPLE.

ID	$\alpha_{J2000}$	$\delta_{J2000}$	$(g_{475}-r_{625})^a$	$(r_{625}-z_{850})^a$	$(i_{775}-z_{850})^a$	$z_{850}^b$	$r_{hl,z}$	$SFR_{UV}^c$
2707/RG	13:38:26.05	-19:42:30.47	3.42 ± 0.17	-0.61 ± 0.03	0.09 ± 0.03	23.05 ± 0.05	0''62	93.7 <sup>2.71</sup> <sub>1.10</sub>
367	13:38:32.75	-19:44:37.27	1.70 ± 0.06	0.52 ± 0.02	0.07 ± 0.02	23.10 ± 0.02	0''20	94.7 <sup>1.99</sup> <sub>3.99</sub>
1991	13:38:27.84	-19:43:15.19	1.88 ± 0.25	0.43 ± 0.08	0.05 ± 0.07	24.43 ± 0.12	0''42	28.8 <sup>2.08</sup> <sub>2.04</sub>
3018	13:38:24.31	-19:42:58.06	1.73 ± 0.14	0.29 ± 0.06	-0.01 ± 0.05	24.49 ± 0.07	0''20	34.2 <sup>1.19</sup> <sub>1.15</sub>
3216	13:38:22.37	-19:43:32.41	1.86 ± 0.15	0.33 ± 0.05	0.10 ± 0.05	24.54 ± 0.06	0''21	26.3 <sup>0.95</sup> <sub>0.89</sub>
3116	13:38:24.21	-19:42:41.85	1.55 ± 0.14	0.36 ± 0.06	-0.00 ± 0.06	24.67 ± 0.06	0''20	25.4 <sup>0.89</sup> <sub>0.89</sub>
959	13:38:32.67	-19:43:3.673	1.88 ± 0.25	0.55 ± 0.07	0.28 ± 0.07	24.73 ± 0.09	0''23	18.2 <sup>1.19</sup> <sub>1.16</sub>
2913	13:38:23.68	-19:43:36.59	1.77 ± 0.22	0.47 ± 0.07	-0.01 ± 0.06	24.94 ± 0.10	0''26	24.2 <sup>1.11</sup> <sub>1.11</sub>
2152	13:38:26.92	-19:43:27.60	1.56 ± 0.17	0.15 ± 0.08	-0.01 ± 0.08	24.97 ± 0.15	0''32	22.4 <sup>1.74</sup> <sub>1.74</sub>
2799	13:38:24.88	-19:43:7.415	1.72 ± 0.17	0.19 ± 0.07	-0.03 ± 0.07	25.03 ± 0.09	0''18	18.6 <sup>0.97</sup> <sub>0.92</sub>
2439	13:38:25.35	-19:43:43.65	1.69 ± 0.24	0.46 ± 0.09	0.14 ± 0.08	25.08 ± 0.10	0''25	17.7 <sup>0.93</sup> <sub>0.93</sub>
3430	13:38:21.21	-19:43:41.99	1.74 ± 0.22	0.49 ± 0.08	-0.03 ± 0.07	25.10 ± 0.09	0''16	17.0 <sup>0.88</sup> <sub>0.83</sub>
2407	13:38:24.35	-19:44:29.15	1.54 ± 0.21	0.43 ± 0.09	0.04 ± 0.08	25.11 ± 0.11	0''26	15.6 <sup>0.97</sup> <sub>0.98</sub>
2839	13:38:25.90	-19:42:18.39	2.23 ± 0.45	0.75 ± 0.09	0.12 ± 0.07	25.14 ± 0.10	0''15	15.6 <sup>0.92</sup> <sub>0.92</sub>
1252	13:38:31.98	-19:42:37.47	1.57 ± 0.16	0.39 ± 0.07	-0.03 ± 0.06	25.25 ± 0.08	0''11	16.3 <sup>0.70</sup> <sub>0.67</sub>
227	13:38:33.02	-19:44:47.57	1.57 ± 0.17	-0.06 ± 0.09	-0.14 ± 0.09	25.29 ± 0.19	0''23	20.4 <sup>1.15</sup> <sub>1.15</sub>
2710/L9	13:38:25.10	-19:43:10.77	1.78 ± 0.25	0.49 ± 0.09	-0.02 ± 0.07	25.34 ± 0.08	0''14	14.4 <sup>0.60</sup> <sub>0.80</sub>
1815	13:38:29.01	-19:43:3.275	1.67 ± 0.24	0.27 ± 0.11	0.01 ± 0.10	25.50 ± 0.12	0''17	11.8 <sup>0.80</sup> <sub>0.75</sub>
1152	13:38:32.62	-19:42:25.15	> 2.13	0.48 ± 0.14	-0.19 ± 0.11	25.57 ± 0.20	0''28	15.0 <sup>1.28</sup> <sub>1.16</sub>
2755	13:38:24.95	-19:43:16.89	1.78 ± 0.53	0.36 ± 0.19	0.12 ± 0.18	25.59 ± 0.21	0''33	10.3 <sup>0.23</sup> <sub>0.23</sub>
3304	13:38:23.67	-19:42:27.37	1.66 ± 0.33	0.56 ± 0.12	0.08 ± 0.10	25.60 ± 0.12	0''15	10.2 <sup>0.77</sup> <sub>0.77</sub>
1819	13:38:29.61	-19:42:38.19	1.98 ± 0.33	0.39 ± 0.10	0.15 ± 0.09	25.60 ± 0.15	0''14	11.0 <sup>0.97</sup> <sub>0.89</sub>
3159	13:38:22.21	-19:43:50.13	> 1.59	0.49 ± 0.23	0.11 ± 0.20	25.63 ± 0.16	0''41	7.83 <sup>0.92</sup> <sub>0.92</sub>
309	13:38:34.77	-19:43:27.59	1.55 ± 0.27	0.20 ± 0.13	0.06 ± 0.12	25.69 ± 0.15	0''21	10.1 <sup>0.92</sup> <sub>0.73</sub>
1808	13:38:30.04	-19:42:22.51	1.61 ± 0.27	0.36 ± 0.11	-0.10 ± 0.10	25.71 ± 0.12	0''15	10.1 <sup>0.68</sup> <sub>0.68</sub>
3670	13:38:20.73	-19:43:16.32	2.09 ± 0.47	0.50 ± 0.12	0.07 ± 0.10	25.81 ± 0.11	0''14	8.77 <sup>0.57</sup> <sub>0.57</sub>
633/L25	13:38:34.96	-19:42:24.95	1.68 ± 0.33	0.32 ± 0.13	0.00 ± 0.12	25.81 ± 0.15	0''24	9.94 <sup>0.78</sup> <sub>0.78</sub>
2524	13:38:24.47	-19:44:7.263	> 2.01	0.60 ± 0.14	-0.02 ± 0.12	25.86 ± 0.21	0''17	13.3 <sup>0.96</sup> <sub>0.96</sub>
1461	13:38:31.37	-19:42:30.95	> 1.97	0.56 ± 0.15	0.07 ± 0.13	25.89 ± 0.15	0''20	8.22 <sup>0.77</sup> <sub>0.77</sub>
3177	13:38:22.97	-19:43:16.07	1.61 ± 0.35	0.27 ± 0.16	0.12 ± 0.15	25.99 ± 0.23	0''18	8.70 <sup>1.09</sup> <sub>0.97</sub>
1668	13:38:26.93	-19:44:53.25	> 1.82	0.72 ± 0.17	0.16 ± 0.13	25.99 ± 0.16	0''17	5.58 <sup>0.84</sup> <sub>0.84</sub>
358	13:38:32.12	-19:45:4.687	2.00 ± 0.54	0.48 ± 0.15	0.03 ± 0.13	25.99 ± 0.19	0''20	7.87 <sup>0.87</sup> <sub>0.79</sub>
2569	13:38:26.38	-19:42:43.55	1.94 ± 0.44	0.36 ± 0.14	0.03 ± 0.13	26.04 ± 0.15	0''13	7.08 <sup>0.59</sup> <sub>0.59</sub>
3131	13:38:25.27	-19:41:55.49	> 2.15	0.28 ± 0.15	-0.09 ± 0.14	26.04 ± 0.19	0''16	8.29 <sup>0.83</sup> <sub>0.83</sub>
2527	13:38:27.99	-19:41:44.07	1.79 ± 0.29	0.28 ± 0.11	-0.13 ± 0.10	26.11 ± 0.22	0''07	10.8 <sup>0.89</sup> <sub>0.89</sub>
2347	13:38:27.99	-19:42:12.22	1.59 ± 0.40	0.42 ± 0.17	0.32 ± 0.16	26.14 ± 0.19	0''14	5.63 <sup>0.69</sup> <sub>0.69</sub>
2358	13:38:24.12	-19:44:47.21	1.70 ± 0.42	0.36 ± 0.16	-0.12 ± 0.15	26.15 ± 0.16	0''14	6.28 <sup>0.66</sup> <sub>0.66</sub>
307	13:38:32.80	-19:44:46.47	2.02 ± 0.49	0.30 ± 0.15	-0.04 ± 0.13	26.17 ± 0.22	0''15	9.76 <sup>0.89</sup> <sub>0.89</sub>
2989	13:38:22.90	-19:43:59.01	1.93 ± 0.29	-0.17 ± 0.13	-0.22 ± 0.13	26.21 ± 0.15	0''12	6.61 <sup>0.54</sup> <sub>0.54</sub>
552/L21	13:38:33.56	-19:43:36.00	1.50 ± 0.32	-0.00 ± 0.18	-0.16 ± 0.18	26.22 ± 0.19	0''18	4.75 <sup>0.68</sup> <sub>0.68</sub>
507	13:38:34.26	-19:43:12.20	> 1.92	0.78 ± 0.15	0.10 ± 0.11	26.22 ± 0.12	0''12	6.50 <sup>0.44</sup> <sub>0.44</sub>
3564	13:38:23.34	-19:41:51.44	1.82 ± 0.49	-0.05 ± 0.23	-0.02 ± 0.23	26.22 ± 0.29	0''32	6.64 <sup>1.11</sup> <sub>0.83</sub>
540	13:38:33.26	-19:43:49.45	1.85 ± 0.52	-0.07 ± 0.24	-0.08 ± 0.24	26.28 ± 0.26	0''23	5.65 <sup>0.80</sup> <sub>0.80</sub>
2480	13:38:27.25	-19:42:30.43	1.78 ± 0.40	0.26 ± 0.15	-0.04 ± 0.14	26.30 ± 0.21	0''11	8.26 <sup>0.75</sup> <sub>0.75</sub>
2712	13:38:26.54	-19:42:12.01	1.73 ± 0.43	0.48 ± 0.15	-0.10 ± 0.13	26.34 ± 0.18	0''12	7.77 <sup>0.60</sup> <sub>0.56</sub>
2494	13:38:25.39	-19:43:34.79	1.61 ± 0.33	0.32 ± 0.15	-0.14 ± 0.13	26.35 ± 0.19	0''09	6.55 <sup>0.60</sup> <sub>0.60</sub>
2708	13:38:24.13	-19:43:50.55	> 1.94	-0.03 ± 0.23	-0.04 ± 0.23	26.39 ± 0.22	0''23	3.89 <sup>0.75</sup> <sub>0.73</sub>
538/L20	13:38:32.83	-19:44:6.934	> 2.17	0.37 ± 0.15	0.13 ± 0.14	26.44 ± 0.16	0''11	5.12 <sup>0.48</sup> <sub>0.48</sub>
1843	13:38:29.54	-19:42:38.83	1.82 ± 0.44	0.11 ± 0.18	-0.21 ± 0.17	26.47 ± 0.21	0''12	5.44 <sup>0.65</sup> <sub>0.65</sub>
1876	13:38:30.04	-19:42:27.78	> 1.61	0.40 ± 0.23	0.03 ± 0.21	26.48 ± 0.25	0''17	5.05 <sup>0.85</sup> <sub>0.71</sub>
375	13:38:32.71	-19:44:38.30	> 1.58	0.35 ± 0.25	0.09 ± 0.23	26.49 ± 0.27	0''19	2.93 <sup>0.68</sup> <sub>0.68</sub>
1655	13:38:29.52	-19:43:10.60	> 2.02	0.46 ± 0.15	0.27 ± 0.14	26.51 ± 0.18	0''10	4.69 <sup>0.55</sup> <sub>0.55</sub>
1339/L14	13:38:28.72	-19:44:36.98	> 1.88	0.37 ± 0.18	0.24 ± 0.18	26.52 ± 0.18	0''13	4.29 <sup>0.48</sup> <sub>0.48</sub>
286	13:38:34.08	-19:43:58.08	1.63 ± 0.45	0.47 ± 0.17	-0.20 ± 0.14	26.52 ± 0.19	0''10	5.43 <sup>0.50</sup> <sub>0.50</sub>
3133	13:38:23.75	-19:42:56.64	> 1.95	0.16 ± 0.20	0.04 ± 0.19	26.53 ± 0.27	0''14	5.95 <sup>0.80</sup> <sub>0.70</sub>
1800	13:38:29.65	-19:42:39.80	> 1.92	0.16 ± 0.20	-0.01 ± 0.19	26.56 ± 0.26	0''14	3.72 <sup>0.65</sup> <sub>0.65</sub>
3486	13:38:21.49	-19:43:21.68	1.82 ± 0.45	0.23 ± 0.17	-0.06 ± 0.16	26.61 ± 0.21	0''10	4.84 <sup>0.59</sup> <sub>0.59</sub>
2874/L4	13:38:22.46	-19:44:33.67	1.88 ± 0.27	-0.35 ± 0.15	-0.14 ± 0.16	26.68 ± 0.23	0''08	4.83 <sup>0.53</sup> <sub>0.53</sub>
1211	13:38:33.53	-19:42:9.188	> 1.73	0.21 ± 0.24	0.19 ± 0.24	26.72 ± 0.27	0''13	2.39 <sup>0.73</sup> <sub>0.66</sub>
1203	13:38:31.76	-19:42:53.82	1.72 ± 0.45	0.42 ± 0.17	0.04 ± 0.15	26.73 ± 0.26	0''07	4.20 <sup>0.57</sup> <sub>0.56</sub>
2571	13:38:23.70	-19:44:32.20	> 1.75	0.09 ± 0.25	-0.00 ± 0.25	26.76 ± 0.23	0''14	1.63 <sup>0.43</sup> <sub>0.43</sub>
1265	13:38:28.64	-19:44:52.16	> 2.08	0.22 ± 0.18	0.36 ± 0.19	26.82 ± 0.18	0''11	2.38 <sup>0.65</sup> <sub>0.65</sub>
1712	13:38:27.93	-19:44:5.602	1.57 ± 0.25	-0.10 ± 0.14	-0.26 ± 0.14	26.83 ± 0.31	0''09	6.78 <sup>0.60</sup> <sub>0.60</sub>
3013	13:38:24.18	-19:43:3.364	1.54 ± 0.42	0.18 ± 0.21	0.05 ± 0.21	26.85 ± 0.30	0''12	3.79 <sup>0.69</sup> <sub>0.69</sub>
1866	13:38:29.33	-19:42:44.09	> 1.63	0.19 ± 0.26	0.24 ± 0.27	26.86 ± 0.30	0''14	2.75 <sup>0.69</sup> <sub>0.68</sub>
1290	13:38:32.15	-19:42:25.57	> 1.54	0.24 ± 0.26	-0.05 ± 0.24	26.88 ± 0.29	0''17	4.00 <sup>0.56</sup> <sub>0.56</sub>

<sup>a</sup>Isophotal colors. The limits are  $2\sigma$ .

<sup>b</sup>Total magnitudes.

<sup>c</sup>SFR estimated from the UV continuum flux ( $i_{775}$ ).

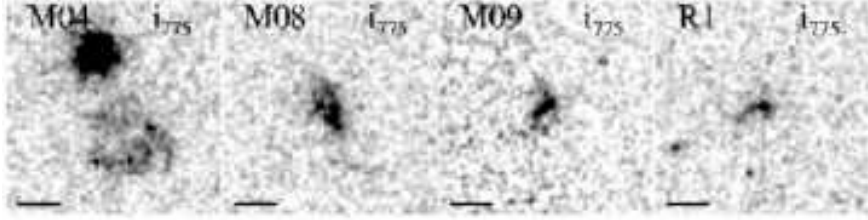


Fig. 19.—  $i_{775}$  postage stamps of MAMBO/VLA sources from De Breuck et al. (2004). The scale bar at the bottom left measures  $1''$ . See text for details on each source.

### A. Properties of MAMBO/VLA sources

De Breuck et al. (2004) studied the protocluster region of TN1338 with deep 20 cm observations obtained with the VLA, and 1.2 mm observations with MAMBO on the 30 m IRAM telescope. They found tentative evidence for an overdensity of candidate mm objects compared to random field surveys. They also found an 11 mJy double-lobed radio source  $\sim 48''$  away from TN J1338–1942, but did not detect it in the mm.

Matching up MAMBO detections with optical/IR counterparts can be difficult given the very wide beams of mm images. The identification of the optical host galaxy can be helped greatly if there is a cm radio detection within the MAMBO search beam, reducing the absolute astrometric uncertainty to only  $\sim 0''.4$ . There are four sources in De Breuck et al. (2004) that are covered by our ACS imaging. If some of the mm sources would be part of the protocluster they would represent a class of highly obscured objects with SFRs up to a few  $1000 M_{\odot} \text{ yr}^{-1}$  (for further details see De Breuck et al. (2004)). However, none of these sources appear to be associated with known LAEs, and none of the MAMBO/VLA sources can be identified with LBG candidates in our sample, although the ACS field size is significantly smaller than the mm field. The  $i_{775}$ -band images are shown in Fig. 19.

**M04** This MAMBO source was identified with a VLA source that has a clear counterpart in our ACS and  $K_S$ -band images. The radio source lies within  $1''$  from a faint spiral structure that can be seen in all bands, approximately  $3''$  south of a relatively bright star. Interestingly, a second, patchy object shows up only in  $i_{775}$  and  $z_{850}$  in between the spiral and the star. A bright object in  $K_S$  encompasses both the spiral and its companion, and its centroid lines up perfectly with the radio source. We measured  $r_{625,AB} - K_{s,Vega} = 4.7$  for the entire system, suggesting that the radio and mm emission arise from an obscured starburst in a merging system at  $z \sim 1$ . The photometric redshift is  $z_B = 0.76_{-0.21}^{+1.11}$ .

**M08** This mm source is possibly associated with an ERO that lies  $6''7$  away. It has not been detected in  $g_{475}$ , and we measured  $r_{625,AB} - K_{s,Vega} = 6.4$ . We have obtained a likely spectroscopic redshift of  $z = 1.18$  (with  $z_B = 1.12_{-0.25}^{+0.25}$ ) based on the detection of faint continuum and OII  $\lambda 3727$ . We classify this source as a dusty, star-forming ERO (e.g. Cimatti et al. 1998).

**M09** The optical/NIR identification of this source is uncertain. The closest object in the ACS images lies  $1''.5$  away from the MAMBO position. This is a faint ( $r_{625}=25.3$ ) object with an elongated shape. It has a featureless SED over all optical/NIR bands observed. The photometric redshift is  $z_B = 0.93_{-0.23}^{+0.45}$ .

**R1** We have identified this 11 mJy double-lobed radio source with a faint optical galaxy ( $r_{625}=25.9$ ). We measured  $g_{475} - r_{625} = 1.2$  and  $r_{625,AB} - K_{s,Vega} = 5.2$ , suggesting either a relatively red object at  $z \sim 1 - 2$ , or possibly an LBG at  $z > 3$ . We find  $z_B = 0.68_{-0.24}^{+3.79}$ . The (observed) optical emission is aligned with the radio axis, most notably in  $i_{775}$ . This is consistent with the alignment seen in other radio galaxies.